

May 2023

Relative Eruption Chronology and Tephra-Vent Correlations of the Sand Mountain Volcanic Field, Oregon High Cascades

Adam S. Chumley
University of Wisconsin-Milwaukee

Follow this and additional works at: <https://dc.uwm.edu/etd>



Part of the [Geochemistry Commons](#), and the [Geology Commons](#)

Recommended Citation

Chumley, Adam S., "Relative Eruption Chronology and Tephra-Vent Correlations of the Sand Mountain Volcanic Field, Oregon High Cascades" (2023). *Theses and Dissertations*. 3130.
<https://dc.uwm.edu/etd/3130>

This Thesis is brought to you for free and open access by UWM Digital Commons. It has been accepted for inclusion in Theses and Dissertations by an authorized administrator of UWM Digital Commons. For more information, please contact scholarlycommunicationteam-group@uwm.edu.

RELATIVE ERUPTION CHRONOLOGY AND TEPHRA-VENT CORRELATIONS OF THE SAND
MOUNTAIN VOLCANIC FIELD, OREGON HIGH CASCADES

by

Adam Chumley

A Thesis Submitted in
Partial Fulfillment of the
Requirements for the Degree of

Master of Science
in Geosciences

at

The University of Wisconsin-Milwaukee

May 2023

ABSTRACT

RELATIVE ERUPTION CHRONOLOGY AND TEPHRA-VENT CORRELATIONS OF THE SAND MOUNTAIN VOLCANIC FIELD, OREGON HIGH CASCADES

by

Adam Chumley

The University of Wisconsin-Milwaukee, 2023
Under the Supervision of Professor Barry Cameron

Tephra stratigraphy east of the SMVF was sampled to characterize the major and trace element geochemistry, along with olivine and plagioclase mineral chemistry, in attempts to correlate the tephra with specific cones and cone groups in the SMVF chain. Three geochemical groups are represented in the tephra stratigraphy, defined by relative proportions of SiO₂, TiO₂, Sr, Cr, and Ni, and determined by SAHN Clustering analysis. These three groups are defined in the basal, middle, and upper portions of the stratigraphy and generally correlate with the three major geochemical groups defined in the SMVF lava flows. Correlation between the tephra and lava flow geochemical subgroups are complicated by magma mixing, magma recharge, heterogeneous crystal growth, sample mixing, tephra reworking, density stratification during fallout, and error during sample preparation for XRF analysis. Regardless, possible subgroup correlations generally agree with the lava flow stratigraphy and interpretations by Deligne et al. (2016) that the Lost Lake Group is the oldest, the Sand Group is second oldest, and the Nash Group is the youngest, while some cones in the Sand Nash Groups were intermittently active around the same time. This refutes radiometric ages produced in the 1960s and 1970's that interpreted the lost Lake Group of cones as the youngest in the chain.

© Copyright by Full Name, 2023
All Rights Reserved

Dedication

This thesis is dedicated to my parents for their unwavering support and encouragement that kept me going throughout my entire academic career, and to Melissa Sikes for her determination, enduring fortitude, and dedication to teaching and the scientific process, all of which served as inspiration for my own research.

TABLE OF CONTENTS

LIST OF FIGURES	vi
LIST OF TABLES	vii
LIST OF ABBREVIATIONS	viii
ACKNOWLEDGEMENTS	ix
Chapter One: Introduction and Baackground	1
Introduction	1
Background	4
High Cascades Volcanism	4
Sand Mountain Volcanic Field	7
Chapter Two: Methods and Results.....	11
Methods.....	11
Field.....	11
Geochemical Analysis.....	14
Results	15
Mineral and Trace Element Geochemistry.....	15
SAHN Cluster Analysis	23
CIA and MIA Analysis.....	29
EMP Mineral Chemsitry	35
Chapter Three: Discussion and Conclusions	11
Discussion	38
Geochemical Variation and Data Scattering	38
Tephra Correlations and Explosive Eruption Chronology	45
Conclusions.....	46
References	50
Appendix A: Trench Photos.....	55
Appendix B: Tephra Geochemistry	59
Appendix C: EMP Mineral Chemistry Tables	60

LIST OF FIGURES

Figure 1	DEM and regional context of the field area	Page 3
Figure 2	Map of SMVF cinder cones and associated lava flows	Page 5
Figure 3	Published ages of SMVF volcanic deposits and lava flows	Page 10
Figure 4	Local context for trenches and samples	Page 12
Figure 5	Simple Sample Stratigraphy	Page 15
Figure 6	Alkali vs. silica and AFM diagrams for all collected samples	Page 19
Figure 7	Master legend for geochemical diagrams	Page 21
Figure 8	Bivariate geochemical diagrams plotting raw tephra and scoria geochemistry against published data	Page 22
Figure 9	SAHN Cluster dendrogram for all collected samples	Page 24
Figure 10	SAHN Cluster dendrogram created from major element data for Medial Trench Tephra	Page 25
Figure 11	SAHN Cluster dendrogram created from trace element data for Medial Trench Tephra	Page 26
Figure 12	SAHN Cluster dendrogram created from major and trace element data for Northern Trench Tephra	Page 27
Figure 13	SAHN Cluster dendrogram created from major and trace element data for Southern Trench tephra	Page 28
Figure 14	Trench tephra color coded and outlined based on SAHN clusters and plotted against published data	Page 30
Figure 15	Tephra geochemistry comparison to published subgroups	Page 31
Figure 16	CIA and MIA analysis diagrams	Page 34
Figure 17	LOI percentage graphs	Page 36
Figure 18	Plots of forsterite percentage against molar MgO and stratigraphic height	Page 37
Figure 19	Plots of molar CaO vs anorthite percentage	Page 39
Figure 20	Bivariate geochemical diagrams showing magma recharge in the published data for the Nash Group	Page 42
Figure 21	Bivariate geochemical diagrams highlighting sample cluster at the end of SAHN Cluster 2.	Page 44
Figure 22a	Northern and Southern Trench stratigraphic columns	Page 48
Figure 22b	Medial Trench stratigraphic column	Page 49
Figure 23	Medial Trench field photos	Page 55
Figure 24	Northern Trench field photos	Page 56
Figure 25	Southern Trench field photos	Page 57
Figure 26	Proximal Trench field photos	Page 58
Figure 27	Bivariate geochemical diagrams of SAHN clusters without SAHN fields	Page 59

LIST OF TABLES

Table 1	Raw tephra and scoria XRF major element geochemistry	Page 16
Table 2	Raw tephra and scoria XRF trace element geochemistry	Page 17
Table 3	Sample list with interpreted published subgroup correlations	Page 32
Table 4	EMP data statistics	Page 37
Table 5	EMP Forsterite percentages for all samples	Page 60
Table 6	EMP Anorthite percentages for all samples	Page 62

LIST OF ABBREVIATIONS

CIA	Chemical Index of Alteration
CLE	Clear Lake East subgroup
CLS	Clear Lake South subgroup
CWC	Cold Water Cove subgroup
EMP	Electron Microprobe
EN I	Early Nash 1 subgroup
EN II	Early Nash 2 subgroup
FTIR	Fourier Transform Infrared Spectroscopy
GS	Great Spring subgroup
IC	Ice Cap subgroup
ICPMS	Inductively Coupled Plasma Mass Spectrometry
LLD	Lower Limit of Detection
LL	Lost Lake Group
MIA	Mafic Index of Alteration
N	Nash Group
OWR	Old Wagon Road subgroup
PCA	Principle Component Analysis
REE	Rare Earth Element
S	Sand Group
SAHN	Sequential Agglomerative Hierarchical Non-overlapping
SMVF	Sand Mountain Volcanic Field
XRF	X-Ray Fluorescence

ACKNOWLEDGEMENTS

I'd like to thank my thesis advisor's Dr. Barry Cameron and Dr. Lindsay McHendry for their continued guidance and encouragement, Chase Glenister for his enormous help in the field, Dr. Gayantha Kodikara and Melissa Sikes for their roles in fixing the XRF at the University of Wisconsin-Milwaukee, and the Geological Society of America and the University of Wisconsin-Milwaukee for funding this research.

Chapter One: Introduction and Background

Introduction

Cinder cones are small, often short-lived basaltic volcanoes that occur as isolated vents, in large fields and chains, and on the flanks of larger volcanoes (Settle, 1979; Conway et al., 1997; Connor et al., 2000, Calvari and Pinkerton 2003; Deligne et al., 2016). Cinder cone volcanism results in continuous or discrete eruption events that last variable periods of time typified by tephra ejection and lava effusion. Cinder cones have been largely interpreted as monogenetic, originating from one parent magma and one period of volcanic activity (Taylor, 1968; Sharrod et al., 2004; Deligne et al., 2016). Eruptions are characterized by lava effusion occurring once the intruding magma has been sufficiently degassed and erupts through the base of the volcanic edifice. However, more recent work over the last twenty years has identified that explosive and effusive eruptions can also occur interchangeably throughout individual cinder cone eruption histories, as well as strombolian eruptions largely forming the cone edifice and explosive strombolian to sub-plinian eruptions depositing tephra (Taddeuci et al., 2004; Valentine et al., 2007; Erlund et al., 2010). Additionally, cinder cone fields and chains can originate from multiple parent magmas and form over longer periods of time from multiple eruption events. As such, their eruption patterns are complex and are heavily influenced by local geologic structure and groundwater presence (Nakamura, 1977; Settle, 1979; Tanaka et al., 1986; Conway et al., 1997; Connor et al., 2000; Taddeuci et al., 2004; Houghton and Gonnerman, 2008; Shea et al., 2010; White and Valentine, 2016; Zawacki et al., 2019; Johnson and Cashman, 2020; Cole et al., 2021).

The Sand Mountain Volcanic Field (SMVF) in the central Oregon Cascades, consisting of approximately twenty cinder cones with associated explosive tephra and lava flows, defines a

north-trending bifurcated lineament that parallels the Horse Creek fault zone on its west side and exists in a graben hosting several shield volcanoes, composite-shields, and cinder cones of Miocene, Pleistocene, and Holocene age (Figure 1). The SMVF cones are approximately 3 ka in age (Taylor, 1968; Deligne et al., 2016) and their conspicuously fine grained deposits have been interpreted as phreatomagmatic (Ruscitto, 2011; McKay, 2012). Cone lineaments influenced by local bedrock structure can erupt in sequences with definable orders in specific directions along the lineaments, as has been observed in the San Francisco Volcanic field in Arizona, or in a less predictable, non-sequential order along the lineaments, as was observed at the 2021 eruption of Fagradalsfjall volcano in Iceland. Additionally, phreatomagmatic phases temporarily exhaust their local water source and typically transition to magmatic phases, which should be evident by fine grained and blocky tephra transitioning to coarse and vesicular tephra through the stratigraphy. Curiously, though lenses of coarse material exist within the SMVF stratigraphy, the tephra is predominantly fine-grained, which suggests a consistent water source for phreatomagmatism (McKay, 2012).

To date, no substantial major and trace element geochemical dataset has been published for the tephra stratigraphy east of the chain and their source vents have not been correlated. However, Deligne et al. (2013; 2016) successfully grouped the cones based on geochemistry of lava and scoria, field relationships, and soil development, and determined a relative eruption sequence for specific cone groups (Figure 2). Identifying the tephra source vents and establishing an explosive eruption sequence for each cone or cone group would help to determine if the tephra-producing eruptions progressed through the lineament in a definable order, or an order mirroring the lava flows, and if specific cones produced the fine-

grained tephra layers in the stratigraphy. Thus, because prior work identified that proximal scoria and lava samples from individual SMVF cones exhibit distinct geochemical signatures

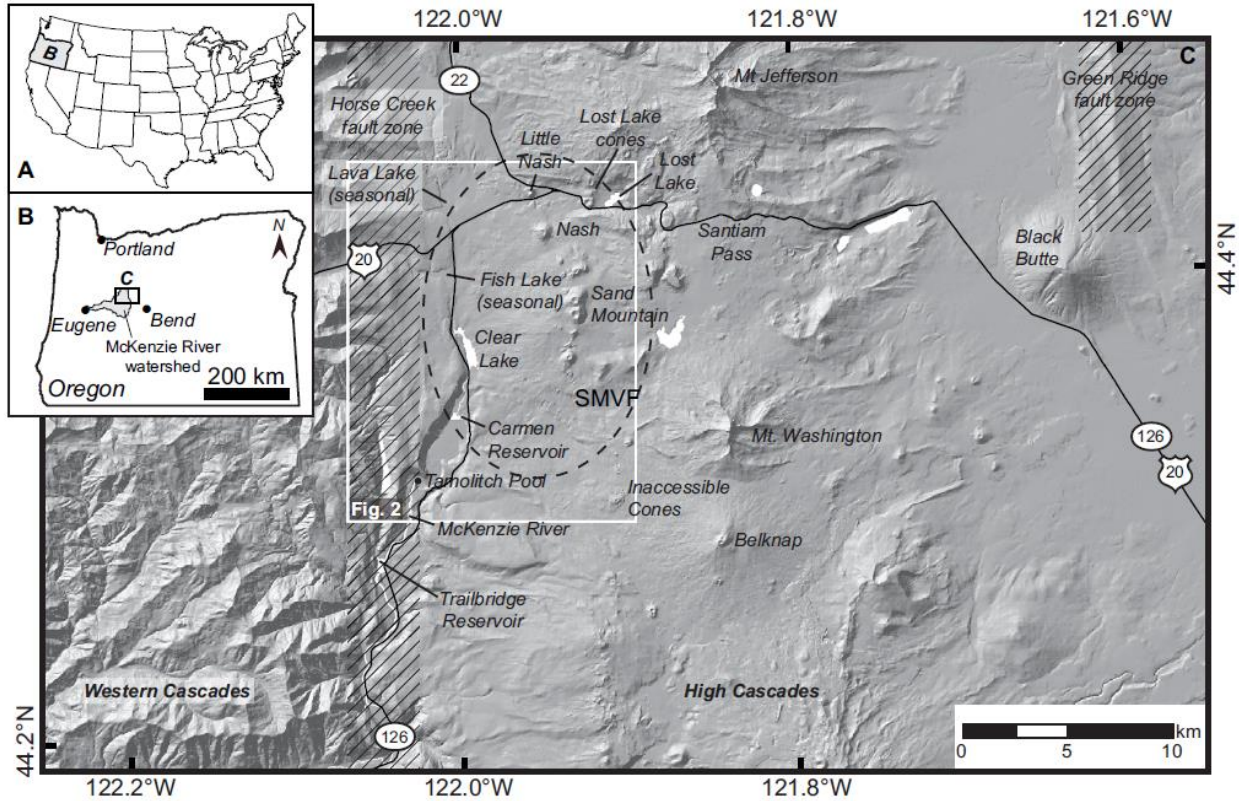


Figure 1. DEM and regional context of the field area (Deligne et al., 2016). A) and B) show the location at the national and state scale. The SMVF (labeled here as the SMVF) is circled in dashed lines and the bounding Horse Creek and Green Ridge fault zones are labeled and represent the fault scarps of the graben.

(Deligne et al., 2016), tephra units with those signatures should indicate the relative temporal sequence of explosive cone activity (Dugmore, 1989; Lowe, 2011; White and Valentine, 2016; Lowe et al., 2017). Therefore, the overriding objective is to determine the relative eruption chronology of the SMVF through tephra correlation.

This work is important for local volcanic hazards assessments, as cinder cone fields commonly lay dormant for thousands of years between eruption events (Conway et al., 1997; Connor et al., 2000; Dzurisin et al., 2009) and nearby South Sister Volcano has experienced

renewed uplift due to magma recharge for more than twenty years (Scott et al., 2001; Wicks, 2002; Lisowski et al., 2021). South Sister volcano and the SMVF do not share the same magma reservoir and produce distinctly different eruptive products, but their proximity suggests regional magmatism is still active and future volcanism in the vicinity of the SMVF could occur. If the Sand Mountain area experiences a similar recharge event, local infrastructure, such as Hoodoo Ski area and Santium Junction, which is adjacent to the northern most cone in the chain and serves as an important highway between Bend, Oregon, and other high-density population centers to the west, could be significantly impacted. Additionally, cinder cones have traditionally been thought to erupt only mildly explosively, grading into effusive eruptions toward the end of their eruptive phases. Only recently have geologists begun to understand that they can erupt more violently (Büttner et al., 1999; White and Valentine, 2016; Zawacki et al., 2019). To understand the hazard potential for future regional basaltic volcanism, a full characterization of the explosive eruptions from the SMVF is necessary.

Background

High Cascades Volcanism

Mafic volcanism in the High Cascades results from decompression melting induced by arc extension and rotation of the North American Plate as the Juan De Fuca Plate obliquely subducts beneath it at the Cascadia Subduction Zone (Hughes and Taylor, 1986; Hughes, 1990; Wells and McCaffrey, 2013). This volcanism typifies the volcanic products in this region and, while larger composite edifices such as the Three Sisters Volcanoes (North, Middle, and South) exist, cinder cones are the most common eruptive vent types. Numerous cinder cones are found either aligned with extensional bedrock structures, on the flanks of stratovolcanoes such as North, Middle, and South Sister Peaks, or as isolated cones, such as Belknap crater. High

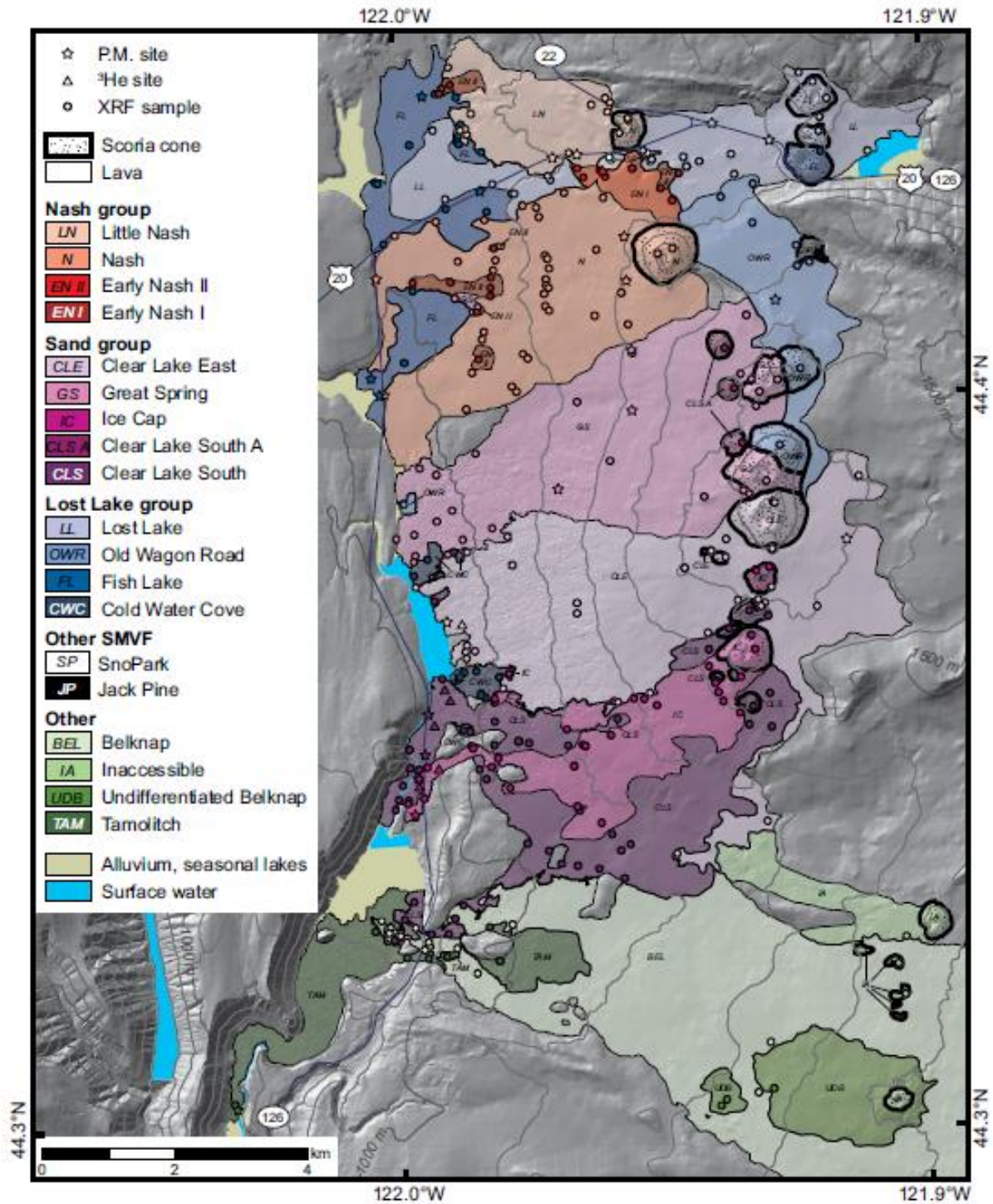


Figure 2. Map of SMVF cinder cones and associated lava flows by Deligne et al., (2016). Sample locations of Deligne et al (2016) are shown on the map as indicated in the legend. These flows and cones were largely grouped into the Nash, Sand, and Lost Lake groups. Belknap crater, a cone not associated with the SMVF is mapped to the south.

Cascade lavas filled in a graben-formed depression creating a mafic platform and were sourced from overlapping shield volcanoes and associated cinder cones during the Pleistocene and Holocene (Taylor, 1978; Smith and Taylor, 1983; Smith et al., 1987). The lavas have largely buried late Miocene and Pliocene volcanic material produced by early High Cascades eruptions, the deposits of which comprise the Deschutes Formation (7.5-4 Ma; Smith and Taylor, 1983; Hughes, 1990; Pitcher et al., 2021), exposed in Green Ridge and representing the eastern fault scarp north of Black Butte.

Hughes and Taylor (1986), and Hughes (1990) obtained geochemical data from several basalts and basaltic andesites sampled in the platform lavas, noting the basalts are tholeiitic with high wt. % TiO_2 and the basaltic andesites are calc-alkaline with lower REE (Rare Earth Elements) than the basalts. The basaltic andesites were further subdivided into two geochemical groups based on TiO_2 , alkali (K_2O plus Na_2O), and REE abundances, with MW types (Mount Washington) exhibiting higher TiO_2 , alkalis, and REE abundances than NS types (North Sister). Their interpretation is that the primitive mineralogy and lower REE of the basaltic andesite relative to the basalts precludes an evolutionary relationship with the basalts, suggesting they originated from different primary magmas that may have undergone differentiation processes other than fractionation (Hughes, 1990). Additionally, the basalt geochemistry suggests they were formed in an extensional regime while the basaltic andesites may have formed during extension with influence from subducted slab derived fluids. This is consistent with the proximity of the arc spreading center to the subduction zone likely creating a multiplicity of magma compositions as they are influenced from both flux melting of the

upper mantle (subduction zone) and from upwelling and decompression melting of a lower source region within the mantle (arc extension; Hughes and Taylor, 1986).

Sand Mountain Volcanic Field

More than twenty distinct cinder cones and forty identifiable vents comprise the SMVF (Taylor, 1965). The Sand group includes cones in the central and southern portions of the chain, the Nash Group includes Nash Crater and Little Nash cones on the northwestern lineament, and the Lost Lake Group includes cones in the upper central and northern lineament portions of the chain. Bifurcation into the two lineaments occurs in the upper central portion where two cone/vent clusters are interpreted by Deligne et al. (2016) to have vents from the Sand and Lost Lake groups. The southern of these two vent clusters is the northern Sand Mountain cone, and the northern of the two vent clusters is a slightly off-axis east-west trending cluster of four distinct overlapping vents, the eastern-most of which is attributed to the Lost Lake Group and the rest attributed to the Sand Group. Taylor (1965) described this vent cluster as the Central Group and the rest of the cones to the south as the Southern Group (Sand Group in Deligne et al., 2016). The two central Sand Mountain cones, Sand Mountain north and Sand Mountain south, are the largest cones in the SMVF (~230 m) and are the most visibly striking features of the chain. Lava generally flowed west, where the topography slopes at an increasing gradient toward the McKenzie River. Lava flows from the Clear Lake South and Ice Cap flows, part of the Sand Group in the south, flowed far enough to dam the McKenzie River (Taylor, 1965; Deligne et al., 2016). Similarly, a lava flow from the Lost Lake cone on the northern lineament, for which the Lost Lake Group is named, dammed Lost Lake to the east. Lava flow and scoria geochemical data published by Deligne et al. (2016) shows the SMVF lavas as calc-alkaline basalt to basaltic andesite in composition and SiO₂ contents from ~48-54 wt.%.

McKay (2012) provides a detailed physical description of the tephra deposit produced by the SMVF. The eruptions dispersed a tephra volume of $\sim 0.39 \text{ km}^3$ over a total area of $\sim 154 \text{ km}^2$, encompassing a deposit considerably larger than other nearby cinder cone deposits to the south. Dominantly fine-grained and finely laminated tephra layers are interlayered with coarse grained layers that encompass the thicker laminations in the deposit. The base of the stratigraphy is marked by a clay layer and the deposit is capped by heavily rooted and reworked tephra. In SEM imagery (Scanning Electron Microscope), tephra are blocky with microfractures and few vesicles. Additionally, Jefferson (2006) studied groundwater paths and sources local to the SMVF and discovered a prominent groundwater system flowing through the permeable lava flows and sourced by high rainfall. This makes sense with the interpretation from McKay (2012) that a consistent water source is required to produce a phreatomagmatic deposit of this volume and consistency. Few geochemical data are available for the SMVF tephra, with studies limited to three individual samples from the McKay (2012) type section (stratigraphic position of samples are not described), and eight individual samples of tephra from pits dug into tephra deposited west of the SMVF on top of multiple lava flows with different source vents (Deligne et al., 2013). McKay (2012) attempted to correlate stratigraphy from local lakes to the SMVF, noting high variability in the major element composition compared to the trace element composition. Deligne et al. (2013) attempted to correlate tephra deposited west of the chain with SMVF lava flows in efforts to determine the contribution of weathered lava flow material to soil development, thereby aiding studies using volcanic soil development as a proxy for relative age. They noted significant data scatter on major and trace element geochemical diagrams, causing difficulty in correlation. Tephra samples from the McKay (2012) type section

range from ~50.6-50.8 wt. % SiO₂ and tephra samples from Deligne et al. (2013) range from ~45-51 wt. % SiO₂.

The SMVF lavas and tephra from the Sand Mountain cones have ages spanning multiple centuries based on carbon dating of charcoals and radiogenic elements in lava flows. Taylor (1965; 1968; 1990) dated a lava flow near Mackenzie and Santium passes to 3,850±215 ¹⁴C yr B.P., but did not source this lava flow to a particular vent in the chain. A charcoal sample found between the top of the SMVF tephra and bottom of the nearby Blue Lake tephra was dated to 3,440±250 ¹⁴C yr B.P., establishing a minimum age for the SMVF tephra deposited in that area. Two other charcoal dates, one at 2,750±45 ¹⁴C yr B.P. for the Clear Lake lava flows and one at 2,590±150 ¹⁴C yr B.P., were reported by Licciardi (1999). Taylor (1968) also dated the Lost Lake group to less than 1,950±150 ¹⁴C yr B.P., which is the youngest reported age for any vent in the SMVF. A compilation of these dates with error bars are depicted in Figure 3.

Deligne et al., (2016) determined cosmogenic He³ dates for seven lava flow samples near Clear Lake, with six samples yielding dates from 3.1 to 2.7 ka and one sample outlier yielding a date of 7.4±0.5 ka. This, corroborated by stratigraphic relationships between flows, establishes an eruption sequence for the lava flow-forming eruptions in the chain, with the Lost Lake group vents defined as the oldest, the Clear Lake group as the second oldest, and the Nash group as the youngest. This contrasts with the published 1,950±150 ¹⁴C yr B.P age from Taylor (1965) as the youngest reported age for the Lost Lake group. However, paleomagnetic data also published by Deligne et al. (2016) suggests no more than 100 years could have passed between the lava flow-forming eruptions from the SMVF. This is inconsistent with the data reporting ages between 3.1 and 2.7 ka. Additionally, He³ cosmogenic dating is sensitive to changes in

contact with direct sunlight. Considering the Sand Mountain area receives significant snow, and likely received more in the past (McKay, 2012), the He³ dates are probably underestimates. The charcoal dates discussed in Sharrod et al. (2004) and reported in Taylor (1965; 1968), Chatters (1968), and Licciardi (1999), were collected in few ash layers and inconsistently described as originating from specific vent groups or from other young flows in the area. As such, established ages and relative eruption sequences are not soundly defined.

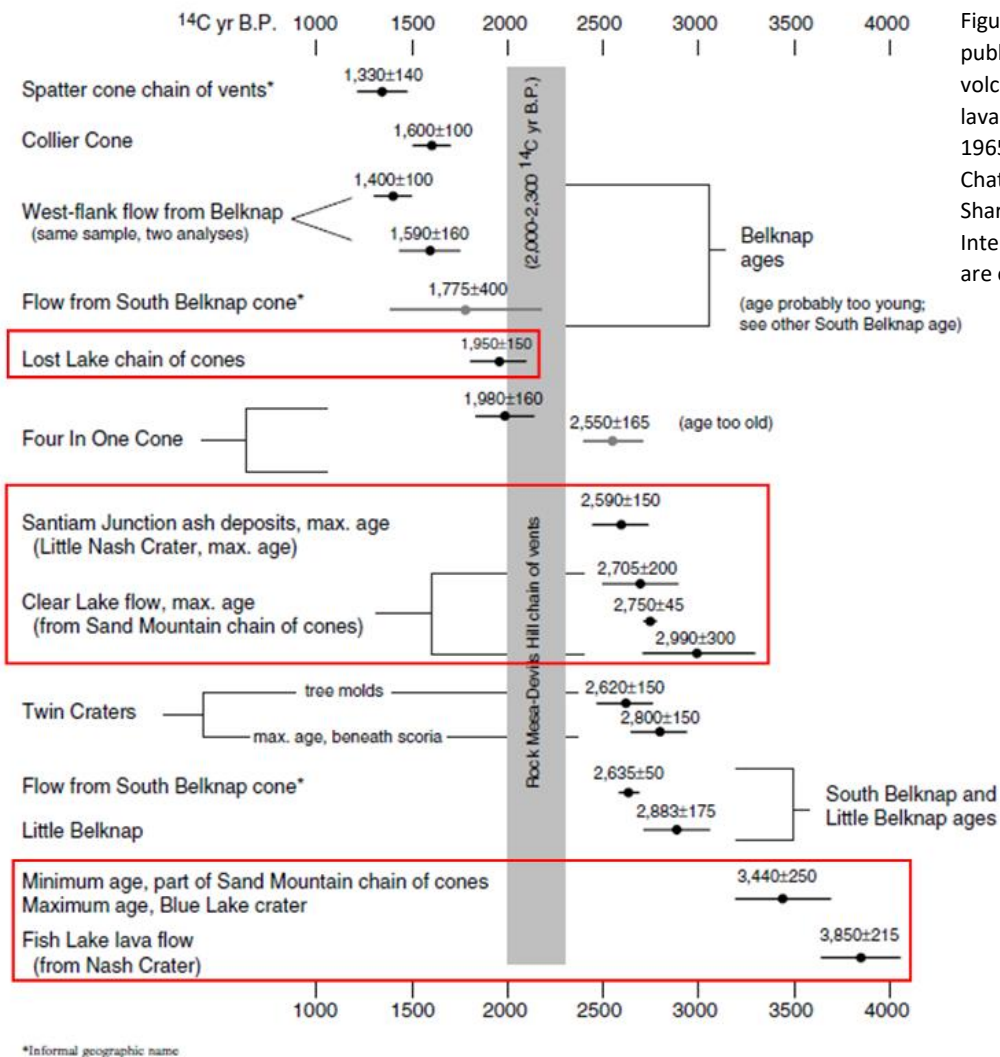


Figure 3. Compiled published Ages of SMVF volcanic deposits and lava flows (Taylor, 1965; Taylor, 1968; Chatters, 1968) via Sharrod et al., 2004. Interpreted SMVF dates are outlined in red.

Methods

Field Methods

Sixty-two tephra samples were collected in September 2021 and August 2022 from volcanic stratigraphy exposed in five ~100-200 cm deep trenches dug east of the SMVF and nine scoria samples were collected atop nine cinder cones across the chain (one sample per cone). Sample stratigraphy for tephra samples analyzed in this study are shown in Figure 5. Trenches were dug with a shovel and tephra and scoria samples were collected with a trowel (Figure 4). Trench locations were selected based on two main criteria: 1) proximity to northern, central, and southern cones in the chain to obtain a sample set representative of all cones and cone groups and 2) amount of vegetative cover to more easily distinguish between capping organic soil and upper volcanic tephra layers. The Northern and Medial trenches were dug to the clay layer at the base of the stratigraphy, but tephra stratigraphy in Southern and Proximal trenches was too thick to dig through in sufficient time. As such, the bottom clay layer was never reached in those trenches. The Medial Trench was dug close to type section from McKay (2012) for comparisons to their stratigraphy. See Appendix A for trench photos.

The stratigraphy of each trench was described from base to top of trench and each section was incrementally measured with a measuring stick. Photos were taken at each increment to visually document the entire stratigraphy and tephra units were delineated by changes in grain size, degree and width of stratigraphic layering, and color. Tephra layers were individually sampled when possible, however many layers were too finely bedded to individually sample, undoubtedly causing those samples to be mixed. Trenches that showed no distinct layering or layering that was too fine to sample throughout the entire section were sampled at consistent measured increments from bottom to top of section. Scoria sampling

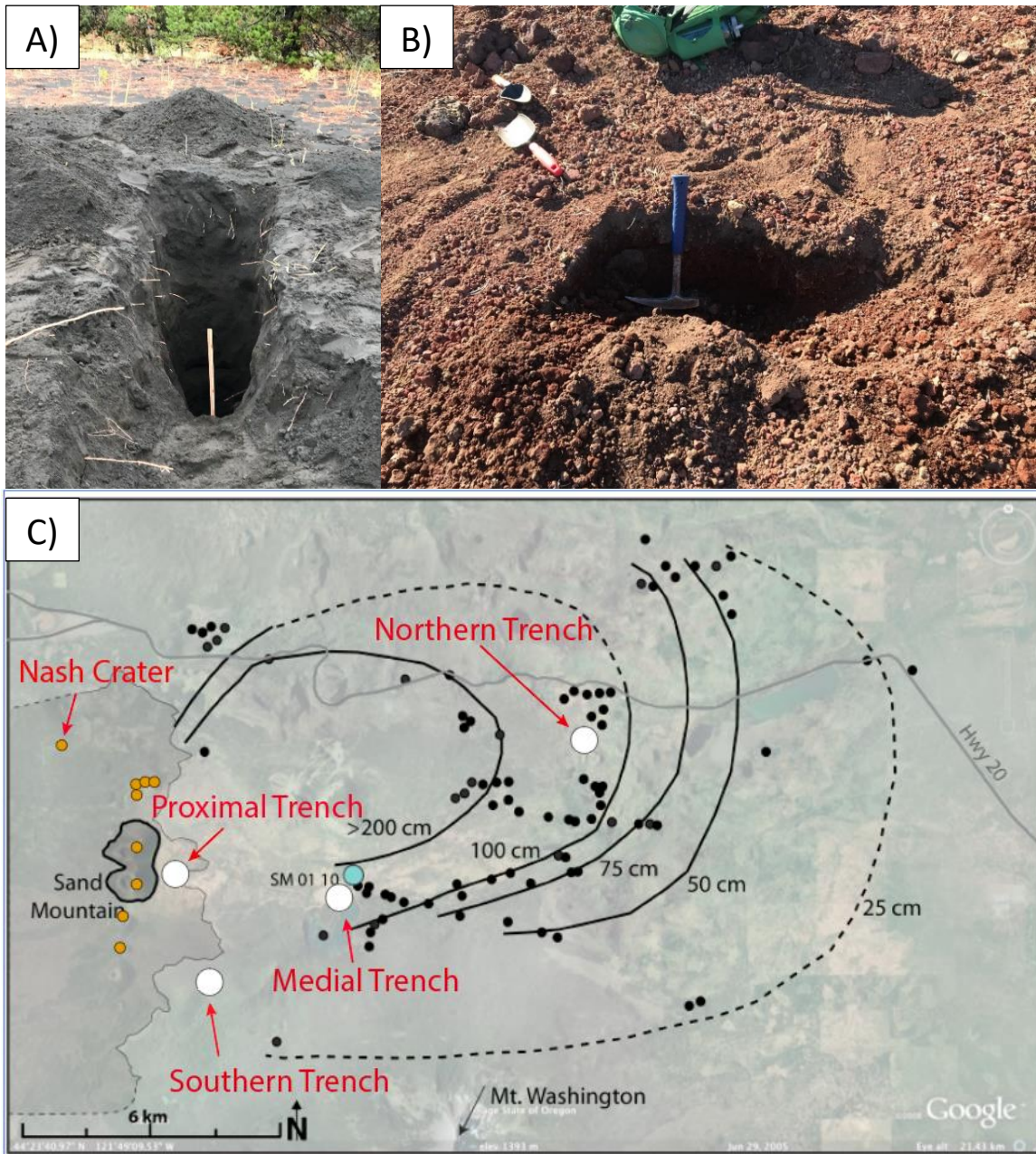


Figure 4. Local context for trenches and samples. A) example of tephra trench (Proximal Trench). B) example of scoria sampling site on cinder cone rim. C) Isopach map of the tephra immediately east of the SMVF from McKay 2012. The black circles are locations of thickness measurements and the light blue circle is the type section, both from McKay, (2012). The orange and white circles are samples collected and analyzed for this work and represent cone rim scoria and tephra trench sampling sites respectively.

sites on cinder cone rims were chosen based on degree of oxidation and sample pits were dug through oxidized surface material into darker, fresher material, though oxidized scoria was not

always possible to avoid. See figures 23-26 in Appendix A for photos of all four trenches discussed here-in.

86 cm Southern Trench	85 cm Northern Trench	151 cm Medial Trench
SMS07_22s	SMN09_21f	SMM16_21f
SMS06_22s	SMN08_21f	SMM15_21f
SMS05_22s	SMN07_21f	SMM14_21f
SMS04_22s	SMN06_21f	SMM12_21f
SMS03_22s	SMN05_21f	SMM11_21f
SMS02_22s	SMN04_21f	SMM10_21f
SMS01_22s	SMN03_21f	SMM09_21f
	SMN02_21f	SMM08_21f/ SMM17_21f
	SMN01_21f	SMM07_21f
		SMM06_21f
		SMM05_21f
		SMM04_21f
		SMM03_21f
		SMM02_21f
		SMM01_21f

coarse ash

Figure 5. Sample stratigraphy for the SMVF tephra. Samples are listed from base to top of stratigraphy in each trench. The medial trench stratigraphy was the deepest of the three main trenches analyzed and contained a thick coarse ash layer at about 60- 86 cm from base.

Geochemical Analysis

Tephra and scoria samples were processed for analytical methods including x-ray fluorescence (XRF) and electron microprobe (EMP). XRF major and trace element geochemical data from the tephra are compared to published XRF geochemical datasets provided by Deligne et al. (2013; 2016) generated from lava and scoria samples collected on and/or near each cone. The EMP at the University of Wisconsin-Madison EMPA laboratory was used to document changes in mineral chemistry through the tephra stratigraphy and between cinder cones.

Samples were processed for x-ray fluorescence (XRF) analysis using the preparation method outlined by Byers et al. (2016). Processing began by powdering the samples in a shatterbox for four minutes each, then heating approximately one gram of each sample to 1,050 °C in a muffle furnace for calculating loss on ignition (LOI). One gram of each sample was then mixed with ten grams of 50/50 lithium tetraborate/metaborate flux with a LiBr non-wetting agent and one gram of ammonium nitrate and fused in a Classie M4 fluxer. Fused beads were analyzed using a Bruker AXS Inc. Pioneer S4 Wavelength Dispersive X-Ray Fluorescence Spectrometer (WD-XRF). For EMP analysis, small holes were drilled into four 25 mm wide sample mounts, then glass shards and olivine grains were carefully picked and placed into each drilled hole, then bound with an epoxy resin. Once the epoxy set overnight, the surfaces of the mounts were polished using polishing paper grit sizes 60-1 µm and then carbon coated by evaporation carbon coating at UW-Madison. Locations on olivine and plagioclase were chosen for analysis based on degree of polishing. Grains that appeared smooth with fewer fractures/scratches were prioritized. Plagioclase microlites smaller than the electron beam were avoided. Cones exhibiting similar mineral chemistry (EMP) and major/trace element (XRF) trends as the tephras are inferred to represent source vents for those tephras.

Results

Major and Trace Element Geochemistry

Tables 1 and 2 list the major and trace element geochemistry for all analyzed tephra samples. Only trace element data with statistical errors below 12% and concentrations more than twice the LLD were accepted for interpretative work. Detected elements include Sr, Ni, Zr, V, Zn, Cr, Ce, and Ba. Zn was not detected in sample SMM01_21f. Notably, the summed percentages, after calculating LOI, range from 96.53 to 100.25 and LOI% ranges from 0.07 to 1.29. Sample SMM01_21f has an anomalous LOI% of -0.04, which is reviewed in the Discussion Section. All samples are calc-alkaline on an AFM diagram (Figure 6b), in agreement with the published lava dataset and consistent with arc rift settings. SiO₂ content ranges from 49.82 to 52.71 wt.% and total alkali content ranges from 3.87 to 4.32 wt.%, defining a compositional range from basalt to basaltic andesite as shown in Figure 6a. Samples SMS01_22S through SMS05_22S from the Southern Trench, which did not reach the basal clay layer, plot in the Basaltic Andesite field in agreement with the published lava flow and cone data where a significant portion of the Sand (Clear Lake East and Great Spring sub-groups) and Nash Groups (Little Nash, Early Nash 1, Early Nash 2 sub-groups) cluster in the basaltic andesite field.

The symbol legend for geochemical diagrams is in Figure 7. Major and trace element concentrations for tephra, scoria, and published datasets are plotted against each other in Figure 8a-f. The published lava flow and scoria data were plotted first and then three major geochemical groups defined by Deligne et al. (2016) were outlined as fields for comparison to the tephra data. Overall, the tephra data display significant scatter across all diagrams in that few data points consistently plot within the published geochemical groups and subgroups. Regardless, a few initial correlations are possible when comparing to the three major

Table 1. Raw XRF major element geochemistry for the tephra and scoria collected in this study. Data is reported as wt.% oxide.

Sample	Location	Sample Type	Na2O	MgO	Al2O3	SiO2	P2O5	K2O	CaO	TiO2	FeO	Fe2O3	LOI (%)	Sum (%)
NC01-21FA	Nash Group	Cone Rim	3.25	5.64	17.76	49.1	0.35	0.61	7.82	1.35	8.45	9.39	0.91	96.53
SMM02-21FA	Lost Lake Group	Cone Rim	3.26	8.16	15.66	49.79	0.3	0.73	8.8	1.4	8.36	9.29	0.72	98.68
SMM03-21FA	Unknown	Cone Rim	2.98	7.87	15.98	49.98	0.32	0.82	8.35	1.25	8.19	9.1	0.20	97.51
SMM04-21FA	Sand Group	Cone Rim	2.89	8.88	15.1	49.97	0.32	0.79	8.11	1.18	8.17	9.08	0.20	97.37
SMM05-21FA	Sand Group	Cone Rim	2.93	8.35	15.38	50.12	0.32	0.82	8.2	1.19	8.07	8.97	0.14	97.14
SMM06-21FA	Sand Group	Cone Rim	3.36	6.62	16.59	52.36	0.32	0.81	8.7	1.22	7.6	8.45	0.14	99.08
SMM07-21FA	Sand Group	Cone Rim	3.1	7.47	16.28	51.9	0.34	0.91	8.96	1.27	8.04	8.93	0.23	100.08
SMM18-22s	Sand Group	Cone Rim	3.09	6.39	16.86	51.39	0.33	0.94	9.84	1.48	8	8.89	0.26	99.84
SMM19-22s	Sand Group	Cone Rim	2.99	7.12	16.68	50.08	0.34	0.84	9.68	1.59	8.4	9.34	0.49	99.52
SMMM02-21f	Medial Trench	Tephra	3.08	7.72	16.29	50.21	0.32	0.82	9.11	1.42	8.19	9.1	-0.04	98.37
SMMM03-21f	Medial Trench	Tephra	3.22	6.61	16.98	51.59	0.33	0.82	9.07	1.31	7.77	8.63	0.05	98.96
SMMM04-21f	Medial Trench	Tephra	3.32	6.59	16.88	51.92	0.32	0.8	8.8	1.21	7.59	8.43	0.70	99.32
SMMM05-21f	Medial Trench	Tephra	3.38	5.73	17.58	52.71	0.35	0.81	8.86	1.29	7.62	8.47	0.49	100.02
SMMM06-21f	Medial Trench	Tephra	3.37	5.79	17.67	52.5	0.34	0.78	8.89	1.27	7.45	8.28	0.35	99.57
SMMM07-21f	Medial Trench	Tephra	3.28	5.28	17.49	51.68	0.34	0.78	8.65	1.3	7.6	8.45	0.54	98.15
SMMM08-21f	Medial Trench	Tephra	3.28	5.73	17.61	51.85	0.34	0.83	9.13	1.44	7.91	8.79	0.72	100.09
SMMM09-21f	Medial Trench	Tephra	3.32	5.68	17.37	51.48	0.33	0.84	9.18	1.38	7.73	8.59	0.38	98.89
SMMM10-21f	Medial Trench	Tephra	3.24	5.89	17.59	51.76	0.34	0.84	9.21	1.46	7.94	8.82	0.45	99.96
SMMM11-21f	Medial Trench	Tephra	3.09	6.49	16.6	49.97	0.31	0.78	8.84	1.28	7.76	8.62	0.24	96.56
SMMM12-21f	Medial Trench	Tephra	3.13	6.5	17.04	50.78	0.32	0.77	8.86	1.28	7.77	8.64	0.26	97.93
SMMM13-21f	Medial Trench	Tephra	3.26	6.24	17.36	51.18	0.32	0.75	8.71	1.31	7.79	8.66	0.86	99
SMMM14-21f	Medial Trench	Tephra	3.37	5.77	17.46	50.72	0.32	0.74	8.45	1.28	7.69	8.55	0.60	97.6
SMMM15-21f	Medial Trench	Tephra	3.34	5.93	17.44	50.67	0.32	0.74	8.45	1.29	7.82	8.69	0.61	97.82
SMMM16-21f	Medial Trench	Tephra	3.29	5.94	18	51.19	0.34	0.74	8.65	1.36	8.04	8.93	0.15	98.95
SMMM17-21f	Medial Trench	Tephra	3.29	6.4	17.66	50.86	0.33	0.73	8.6	1.32	8.01	8.9	1.29	99.75
SMMM18-21f	Medial Trench	Tephra	3.33	5.7	17.43	51.6	0.34	0.84	9.17	1.39	7.73	8.59	0.49	99.23
SMMN01-21f	Northern trench	Tephra	3.21	6.94	17.36	50.08	0.35	0.76	8.99	1.52	8.83	9.81	0.07	99.45

Table 1 continued.

Sample	Location	Sample Type	Na2O	MgO	Al2O3	SiO2	P2O5	K2O	CaO	TiO2	FeO	Fe2O3	LOI (%)	Sum (%)
SMMN02_21f	Northern trench	Tephra	3.16	7.45	16.63	50.25	0.3	0.71	9.2	1.5	8.35	9.28	0.41	99.25
SMMN03_21f	Northern trench	Tephra	3.29	7.65	16.6	49.82	0.31	0.69	9.08	1.51	8.55	9.5	0.64	99.45
SMMN04_21f	Northern trench	Tephra	3.21	6.08	17.18	50.86	0.35	0.86	9.83	1.67	8.22	9.13	0.97	100.5
SMMN05_21f	Northern trench	Tephra	3.13	5.82	17.48	49.83	0.36	0.85	9.45	1.67	8.5	9.45	1.17	99.55
SMP07_21f	Proximal Trench	Tephra	3.19	6.97	17.37	51.57	0.32	0.7	8.57	1.23	7.84	8.71	0.03	99
SMP08_21f	Proximal Trench	Tephra	3.36	7.33	16.81	51.13	0.3	0.71	8.52	1.19	7.85	8.72	0.26	98.68
SMS01_22s	Southern Trench	Tephra	3.51	5.76	17.41	52.77	0.32	0.81	8.92	1.29	7.54	8.38	0.22	99.74
SMS02_22s	Southern Trench	Tephra	3.41	6.25	17.39	52.35	0.32	0.77	8.75	1.25	7.65	8.5	0.25	99.59
SMS03_22s	Southern Trench	Tephra	3.4	6	17.47	52.39	0.32	0.78	8.78	1.27	7.59	8.43	0.34	99.53
SMS04_22s	Southern Trench	Tephra	3.51	5.48	17.91	52.48	0.34	0.79	8.79	1.31	7.55	8.39	0.36	99.71
SMS05_22s	Southern Trench	Tephra	3.3	6.7	17.18	52.19	0.32	0.76	8.75	1.25	7.75	8.61	0.28	99.68
SMS06_22s	Southern Trench	Tephra	3.34	6.8	17.32	51.59	0.32	0.75	8.64	1.25	7.85	8.72	0.53	99.62
SMS07_22s	Southern Trench	Tephra	3.49	5.86	18.09	51.79	0.34	0.74	8.81	1.33	7.77	8.64	0.82	100.25

Table 2. Raw XRF trace element geochemistry for the tephra and scoria collected in this study. Data is reported in ppm. Summed percentages include both major and minor elements

Sample	Location	Sample Type	Zr	V	Zn	Ni	Cr	Ce	Sr	Ba	Mn
NC01-21FA	Nash Group	Cone	167	221	85	138	109	41	730	377	0.15
SM02-21FA	Lost Lake Group	Cone	145	250	69	165	280	36	694	282	0.15
SM03-21FA	Unknown	Cone	146	217	68	149	244	39	925	364	0.15
SM04-21FA	Sand Group	Cone	144	214	85	178	278	43	887	344	0.15
SM05-21FA	Sand Group	Cone	144	212	66	167	242	37	927	385	0.15
SM06-21FA	Sand Group	Cone	152	215	76	104	134	35	1038	305	0.14
SM07-21FA	Sand Group	Cone	152	229	60	109	217	37	978	361	0.15
SM18_22s	Sand Group	Cone	154	265	64	66	158	42	1032	397	0.15
SM19_22s	Sand Group	Cone	153	254	64	99	206	40	893	324	0.15
SMM01_21f	Medial Trench	Tephra	145	238	ND	125	245	38	814	300	0.15
SMM02_21f	Medial Trench	Tephra	145	230	72	91	174	40	961	345	0.14
SMM03_21f	Medial Trench	Tephra	144	220	75	101	185	40	1019	367	0.14
SMM04_21f	Medial Trench	Tephra	154	223	86	78	128	43	1044	339	0.14

Table 2 continued.

Sample	Location	Sample Type	Zr	V	Zn	Ni	Cr	Ce	Sr	Ba	Mn
SMM05_21f	Medial Trench	Tephra	154	226	74	76	119	37	1049	340	0.14
SMM06_21f	Medial Trench	Tephra	161	253	74	61	121	41	1021	332	0.14
SMM07_21f	Medial Trench	Tephra	159	251	70	78	141	39	984	398	0.15
SMM08_21f	Medial Trench	Tephra	148	231	64	66	127	39	987	337	0.14
SMM09_21f	Medial Trench	Tephra	161	259	61	78	154	40	956	374	0.14
SMM10_21f	Medial Trench	Tephra	153	218	67	98	163	33	933	331	0.15
SMM11_21f	Medial Trench	Tephra	151	235	64	99	160	37	993	369	0.14
SMM12_21f	Medial Trench	Tephra	157	222	68	95	154	38	936	343	0.15
SMM13_21f	Medial Trench	Tephra	151	219	73	93	122	36	912	352	0.14
SMM14_21f	Medial Trench	Tephra	157	225	64	96	136	37	907	329	0.14
SMM15_21f	Medial Trench	Tephra	156	245	63	88	146	39	906	305	0.15
SMM16_21f	Medial Trench	Tephra	157	226	66	93	169	37	946	349	0.15
SMM17_21f	Medial Trench	Tephra	156	235	77	72	140	39	978	320	0.14
SMM01_21f	Northern Trench	Tephra	152	280	55	122	212	37	713	360	0.16
SMM02_21f	Northern Trench	Tephra	143	261	54	116	250	33	726	227	0.16
SMM03_21f	Northern Trench	Tephra	157	257	46	131	264	33	719	259	0.15
SMM04_21f	Northern Trench	Tephra	155	291	65	58	166	38	934	299	0.16
SMM05_21f	Northern Trench	Tephra	163	279	58	59	137	38	871	326	0.15
SMP07_21f	Proximal Trench	Tephra	148	207	64	122	169	38	971	282	0.14
SMP08_21f	Proximal Trench	Tephra	144	196	68	150	157	34	964	270	0.14
SMS01_22s	Southern Trench	Tephra	154	235	60	72	140	37	997	331	0.14
SMS02_22s	Southern Trench	Tephra	155	217	69	94	148	37	979	319	0.13
SMS03_22s	Southern Trench	Tephra	154	224	63	93	131	40	960	328	0.14
SMS04_22s	Southern Trench	Tephra	154	248	41	72	123	36	992	292	0.14
SMS05_22s	Southern Trench	Tephra	154	239	53	118	159	40	963	291	0.14
SMS06_22s	Southern Trench	Tephra	161	223	55	111	160	37	950	319	0.14
SMS07_22s	Southern Trench	Tephra	155	245	47	79	143	34	968	323	0.14

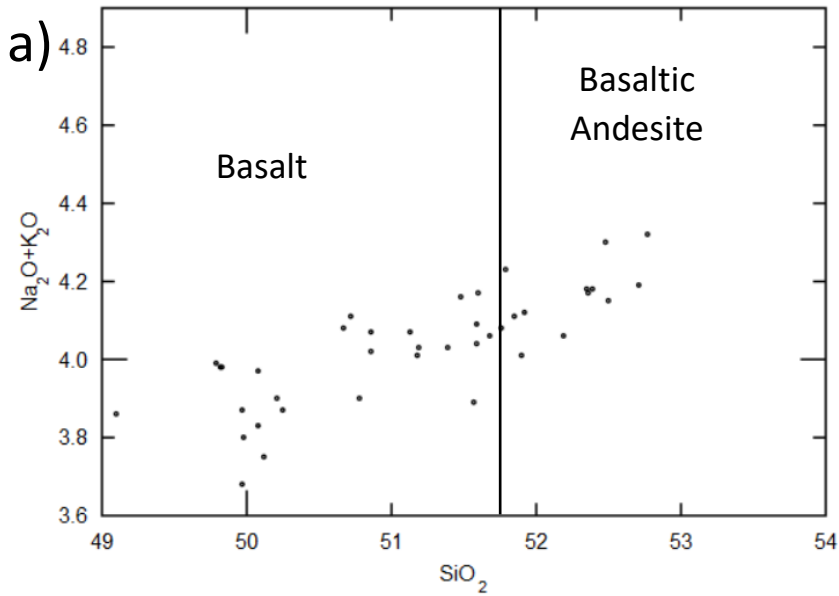
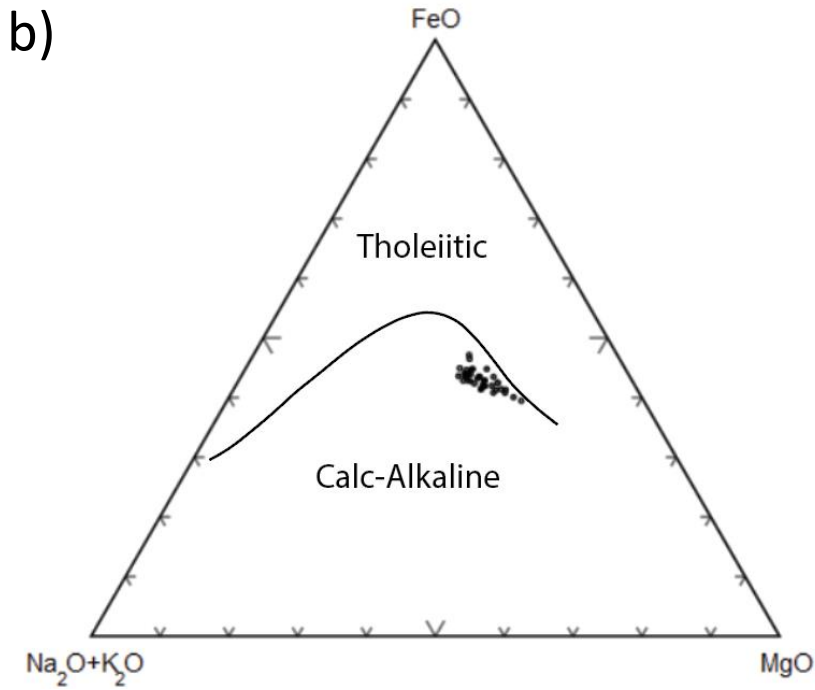


Figure 6. a) Alkali vs Silica and b) AFM diagram of tephra and scoria samples collected in trenches and on cone rims. Most samples are basalt on the alkali vs. silica diagram, with the Southern Trench largely plotting in the basaltic andesite field. All samples are calc-alkaline on the AFM diagram.



geochemical groupings in the published lava flow data. Tephra samples SMM01_21f from the base of the Medial trench and SMN01_21f through SMN03_21f from the base of the Northern trench consistently plot in or near the Lost Lake field, indicating Lost Lake Group or early Sand

Group affinity. Most other samples plot in the Sand Group field and many plot in or near the Nash Group field, but inconsistently. For example, SMS04_22S is the only sample that plots in the Nash field on four out of the six diagrams, indicating a stronger correlation with the Nash Group.

Scoria samples are compared to the published dataset to determine consistency between the published data and data produced here-in. Samples SM02_21f through SM05_21f, collected from cones attributed to the Sand and Lost Lake groups by Deligne et al. (2016), plot in both Sand and Lost Lake fields on different bivariate geochemical diagrams (Figure 8a-f). Samples SM06_21f and SM07_21f were collected from the two central largest Sand Mountain cones, which are assigned to Sand subgroups Clear Lake East (southern cone) and Great Spring (northern cone), but do not plot with either subgroup. Samples SM18_22S and SM19_22S, collected from southern cones, attributed to the Ice Cap and Clear Lake South subgroups respectively, do plot with the Ice Cap and Clear Lake South sub-groups. NC01_21f was collected from Nash Crater at the northern end of the SMVF, and plots with the Nash group on bivariate diagrams of SiO₂ vs. MgO and Sr vs. Cr but is anomalous on many other geochemical diagrams. A lower summed percentage (96%) for this sample may contribute to anomalous plotting.

In general, the scoria data plots with or near the major cone groups from which they were collected, but some samples do not plot with their cones' attributed subgroups, causing difficulty in correlation on the subgroup scale between the tephra and scoria collected in this study. As such, consistency in the published bulk geochemical datasets from Deligne et al. (2013; 2016) provide a more robust base for geochemical comparison and potential correlation than the scoria samples collected here-in.

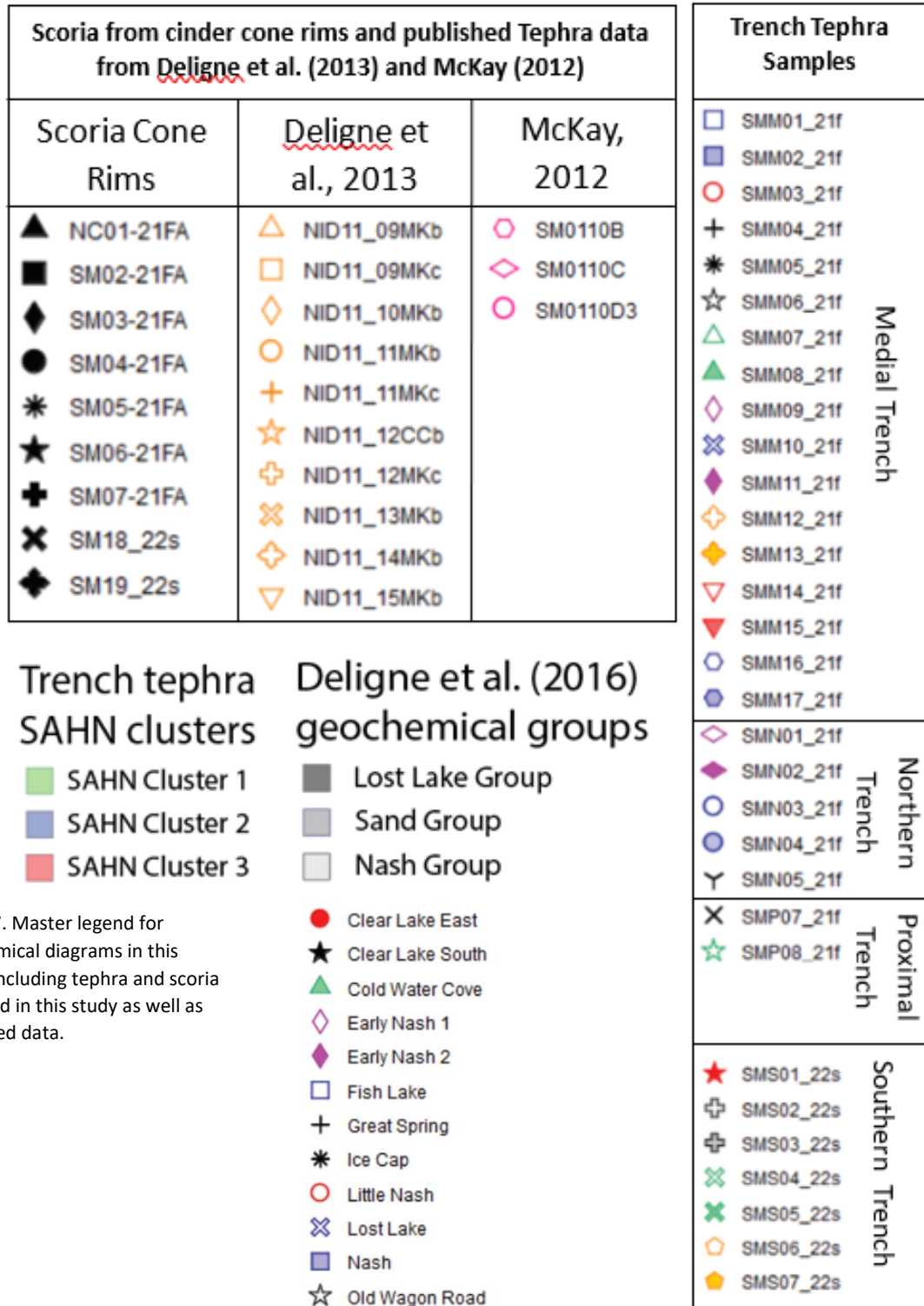


Figure 7. Master legend for geochemical diagrams in this study, including tephra and scoria collected in this study as well as published data.

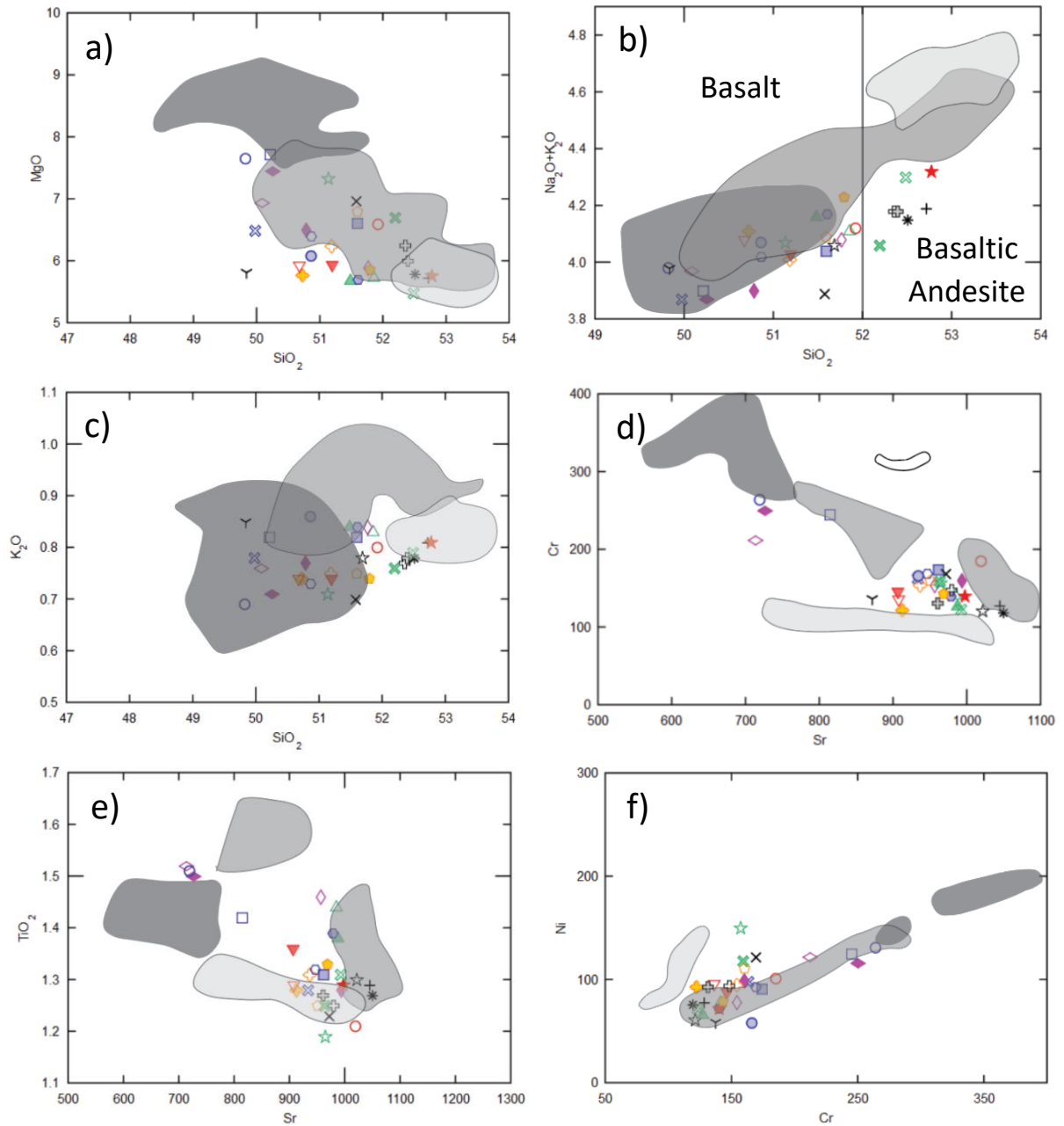


Figure 8. Bivariate geochemical diagrams plotting tephra and scoria geochemistry against published lava flow and scoria geochemistry (published data from Deligne et al., 2016). The legend is shown on top of the next column. Published data are defined by fields outlined in blue, green, and red representing the Sand, Nash, and Lost Lake groups respectively. Selected major oxides and trace elements are the most influential contributors to data variation shown in figure 5a-b.

SAHN Cluster Analysis

Because trends and clustering are difficult to observe in the raw geochemical data when comparing to the published lava flow data, SAHN clustering analyses were performed on the tephra and scoria data to determine if specific groups could be statistically recognized. This analysis follows the mathematical and conceptual framework for hierarchical cluster analyses outlined by Dubes (1998) and was performed using the *vegan* package in R. SAHN clustering analysis is an agglomerative (hierarchical) clustering analysis that determines which individual data points are the most related and groups these data points together defining nested clusters of smaller clusters within larger clusters. These clusters are determined by initially measuring the Euclidian distance between one data point and the next nearest data point for all data, thereby producing pairs of data points that are then averaged. Euclidian distances between each average and the next nearest average are then calculated and grouped together into a larger cluster. Each subsequent cluster is then grouped together in the same way until all data is grouped into one final cluster that is split into multiple smaller clusters. These nested clusters are output as dendrograms. The cophenetic correlation coefficient is also determined in R and represents the accuracy of the clusters in relation to the original dataset. Only values above 0.75 are considered accurate, though this can be subjective if the clusters agree with other data.

SAHN cluster dendrograms were created for all tephra and the three trenches from which geochemical data was produced (Figures 9-13), which are the Medial, Northern, and Southern trenches. Separate analyses were run for major and trace elements to determine if they are consistent with each other. Both major and trace element SAHN cluster analyses

produced three SAHN clusters in the tephra geochemical data that are represented in three portions of the stratigraphy (Figure 10 and 11). Samples SMM02_21f, SMM11_21f, SMS04_21f,

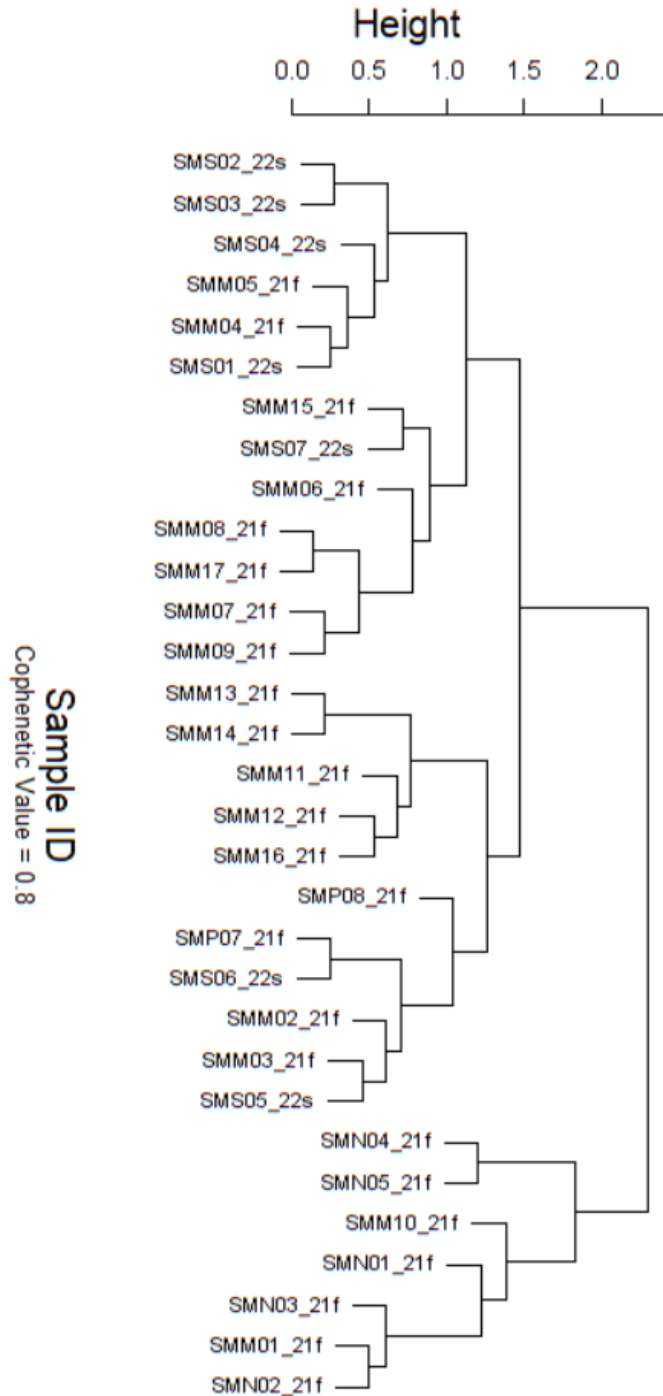


Figure 9. Dendrogram output from a SAHN cluster analysis of all trench tephra samples. Height on the x-axis is a measure of dissimilarity between clusters. The longer the lines connecting clusters into larger groups, the more separated and well defined those clusters are. Tephra do not cluster well enough to distinguish clear correlations.

SMS05_21f, and SMS06_21f cluster

differently on major and trace element cluster analyses (Figures 10-13), but all other samples are consistent between both cluster analyses for each trench.

These clusters are best represented in the Medial Trench, which contains the most complete sampled stratigraphy in this study (Figures 10-11). SAHN cluster 1 is in the bottom portion of the stratigraphy and represents ~6% of the Medial Trench stratigraphy, SAHN cluster 2 is in the lower to middle portion of the stratigraphy and encompasses ~53% of the Medial Trench Stratigraphy, and

SAHN cluster 3 is in the upper portion of the stratigraphy and encompasses ~41% of the Medial

Trench stratigraphy. SAHN cluster 2 is the largest cluster containing the most samples and SAHN cluster 1 is smallest cluster containing the fewest number of samples. The samples

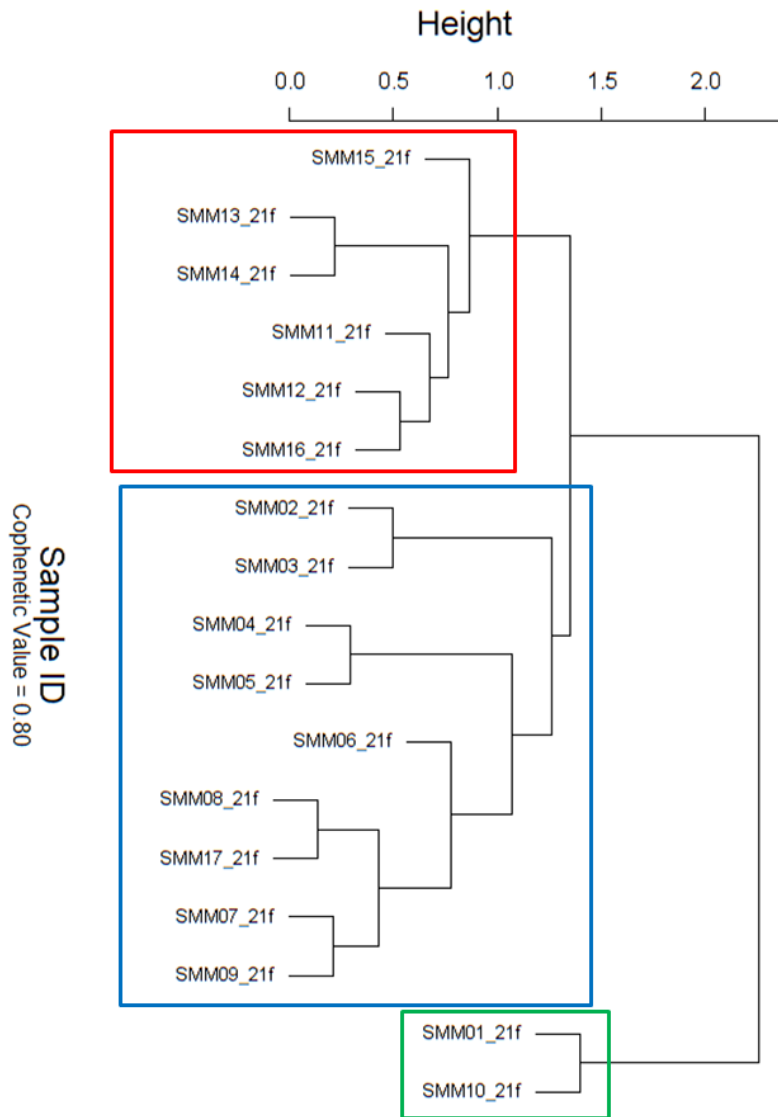


Figure 10. Dendrogram output from a cluster analysis of Medial Trench Tephra based on only major element geochemical data. Three distinct clusters are well defined by the analysis and in the stratigraphy. These are outlined in green for SAHN cluster 1 at the base of the stratigraphy, blue for SAHN cluster 2, and red for SAHN cluster 3.

cluster in a less well-defined way in the analysis that included all trench tephra (Figure 9), and thus was not used to define SAHN clusters in the data. See Figure 27 in Appendix B for geochemistry plots without SAHN Fields.

When color coded on geochemical diagrams, the

three SAHN clusters are clearly visible with variable overlap between clusters 2 and 3 (Figure 14a-f). A few observable changes were made to the clusters output in the SAHN analysis that are consistent across most diagrams. These include samples SMM10_21f and SMS05_21f which most consistently plots with SAHN cluster 2. Additionally, samples SMN04_21f, SMN05_21f,

SMP07_21f, and SMP08_21f do not consistently plot with any specific SAHN cluster on the bivariate plots below, and were color coded differently for this reason. SAHN cluster 1 is the least evolved showing higher MgO, TiO₂, Cr, and Ni contents and

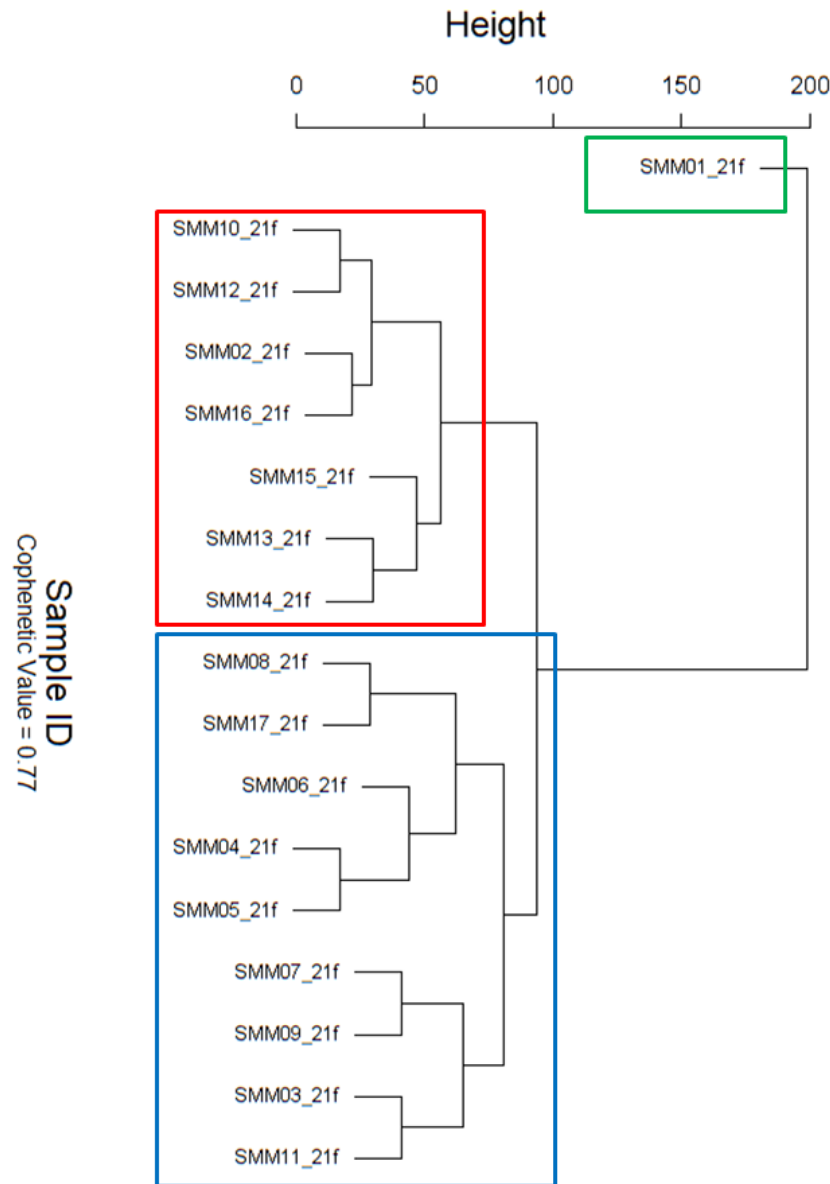


Figure 11. Dendrogram output from a cluster analysis of Medial Trench Tephra based on only trace element geochemical data. The three distinct clusters are slightly less well defined than the major element output. Sample SMM11_21f which is attributed to cluster 2 and samples SMM10_21f and SMM02_21f which are attributed to cluster 3.

lower SiO₂, alkalis, and Sr contents which are common trends in less evolved, more mafic magmas. SAHN Cluster 1 also correlates well with the Lost Lake group and the less evolved portions of the Sand Group, defining the transition between the two groups. Interestingly, SAHN cluster 3 is

less evolved than SAHN cluster 2 on major oxide bivariate diagrams, showing MgO, K₂O, Na₂O, SiO₂, Cr, Sr, and TiO₂ concentrations between SAHN Clusters 1 and 2. SAHN Cluster 3 also does

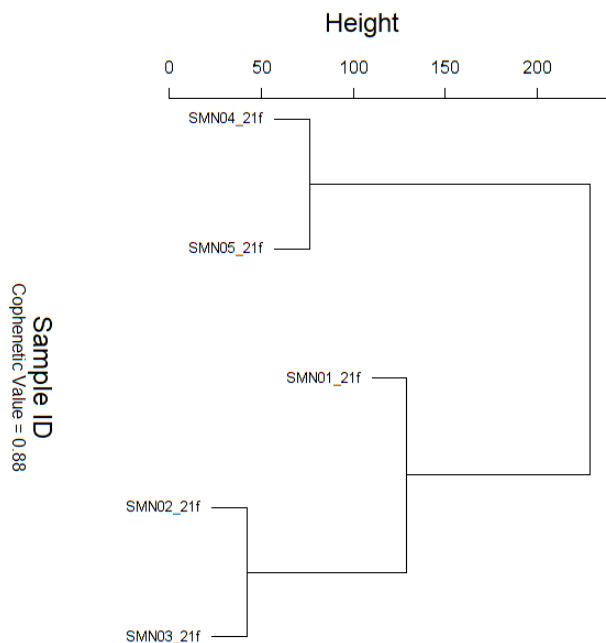
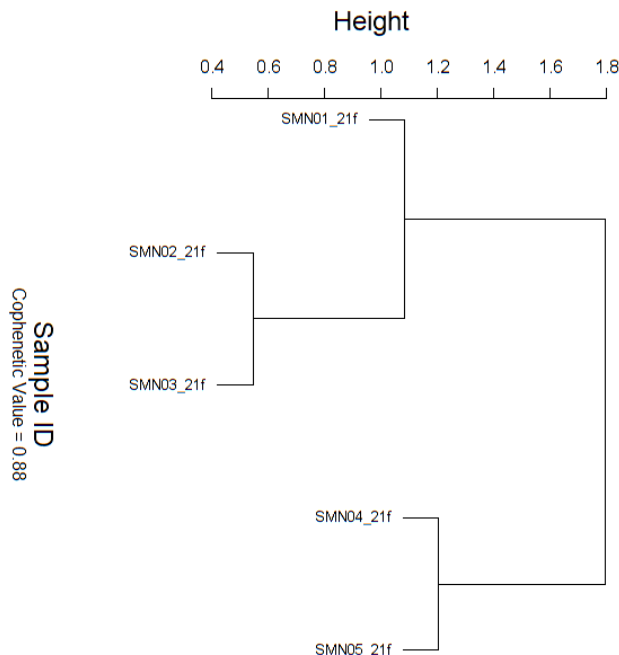


Figure 12. Dendrogram output from a cluster analysis of Northern Trench tephra based on a) major and b) trace element geochemical data. SMN01_21f through SMN03_21f define SAHN cluster 1 while SMN04_21f and SMN05_21f define a second cluster in both diagrams.

not plot with the Nash Group, despite

being the stratigraphically highest

SAHN Cluster where the Nash Group

volcanic products should be best

represented (Figure 14a-c) based on

interpretations of the lava flow

stratigraphy by Deligne et al. (2016).

Trace element bivariate plots of Sr vs.

TiO₂, Sr vs. Cr, and Cr vs. Ni produce

trends more similar to the published lava

flow and scoria data (Figure 14d-f),

showing potential correlation. This

suggests that the trace element

concentrations may have fractionated

differently than the major oxides during magma evolution or simply that they are more

sensitive to fractionation processes than the major elements. When these plots are overlaid

with published tephra data from Deligne et al. (2013; Figure 14a-f), the published tephra data

does not consistently plot with the published lava flow/scoria data or the tephra data produced here-in, suggesting buried vents or post depositional processes. In the case of one trench, Deligne et al. (2013)

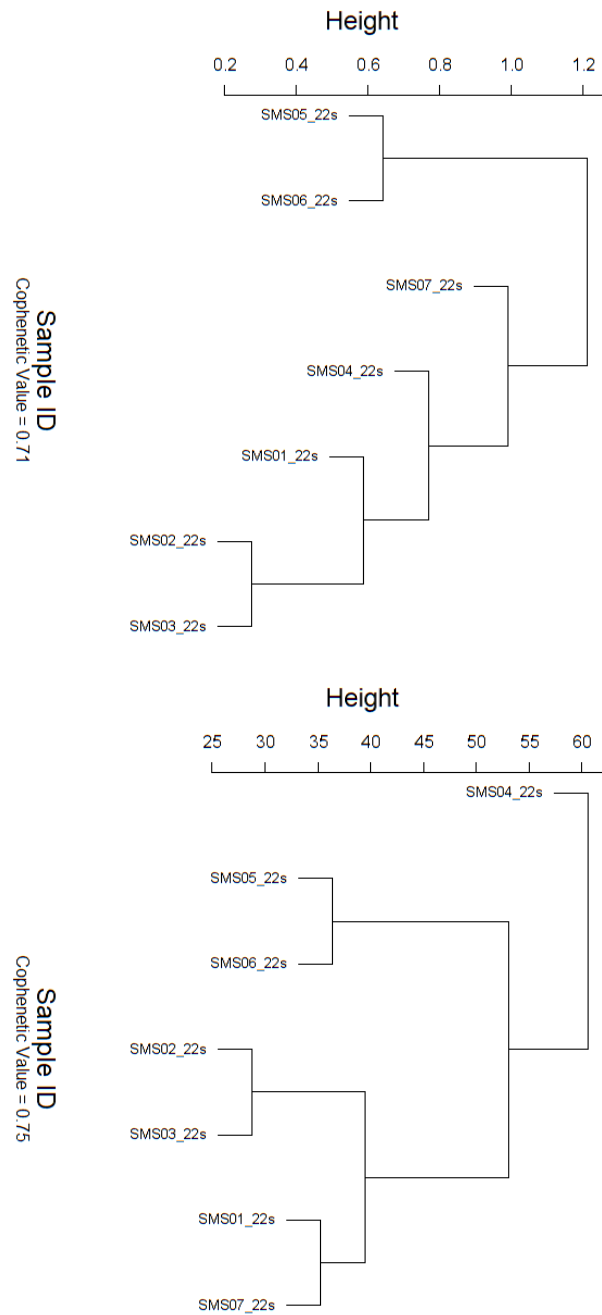


Figure 13. Dendrogram output from a cluster analysis of Southern Trench tephra based on a) major and b) trace element geochemical data. Both analyses show two SAHN clusters, but SMS05_21f, SMS06_21f, and SMS04_21f are attributed to different clusters in both dendrograms. As such, SAHN clusters in the southern trench are less well defined in the analysis.

described a small tephra blanket located west of the SMVF on the Clear Lake East sub-group lava flow as appearing linear similar to a fissure, but no source vents were found.

These SAHN clusters also help to make correlations between the tephra within each cluster and published geochemical subgroups more observable. Figure 15 shows fourteen samples between each trench plotted against the published subgroups. Though no sample plots in the same subgroup on every diagram, plotting is consistent enough to

make potential correlations. These samples and their correlated subgroups are outlined in table

3 while the rest of the SMVF tephra samples do not consistently plot within any subgroup. See the Discussion section for updated stratigraphy as visual aid for correlations between the three major geochemical groups and their subgroups.

CIA and MIA Analysis

The Chemical Index of Alteration (CIA), formulated by Nesbitt and Young (1982), was calculated for all tephra samples collected in this study and lava flow samples published by Deligne et al. (2016) to compare the degree of weathering between the two sample sets and to determine if chemical weathering contributes to data scattering in some geochemical diagrams. CIA analyses compare relative proportions of molar Al_2O_3 to a sum of molar $Al_2O_3+CaO+Na_2O+K_2O$, as Al_2O_3 is more stable in oxidizing environments while CaO, Na_2O and K_2O weather away during feldspar dissolution. However, CIA analysis does not account for MgO or FeO content, the former of which weathers out of mafic rocks in oxidizing environments while the latter becomes enriched in iron oxides. The Mafic Index of Alteration (MIA) defined by Babecheck et al. (2014) incorporates molar concentrations of both MgO and Fe_2O_3 , which serve as major cations for pyroxene and olivine in mafic igneous rocks, into the equation defined by Nesbitt and Young (1982). MgO weathers away in oxidizing environments while ferric iron is stable. The CIA and MIA equations are as follows:

Eq. 1.
$$CIA = \left(\frac{Al_2O_3}{Al_2O_3 + CaO^* + Na_2O + K_2O} \right) * 100\%$$

Eq. 2.
$$MIA_{(O)} = \left(\frac{Al_2O_3 + Fe_2O_3}{Al_2O_3 + CaO^* + Na_2O + K_2O + MgO + Fe_2O_3} \right) * 100\%$$

where:

$$CaO^* = \text{moles of CaO} - (10/3 \times \text{moles of } P_2O_5)$$

CaO* typically includes CO₂ to account for calcite and dolomite, but CO₂ was driven off during the fluxing process and mafic rocks do not commonly contain calcite, so their contribution, if present, is negligible. Tephra CIA values range from ~43 to ~46, while MIA values range from ~34 to ~39, in agreement with low CIA and MIA values in other basaltic rocks (Babecheck et al., 2014).

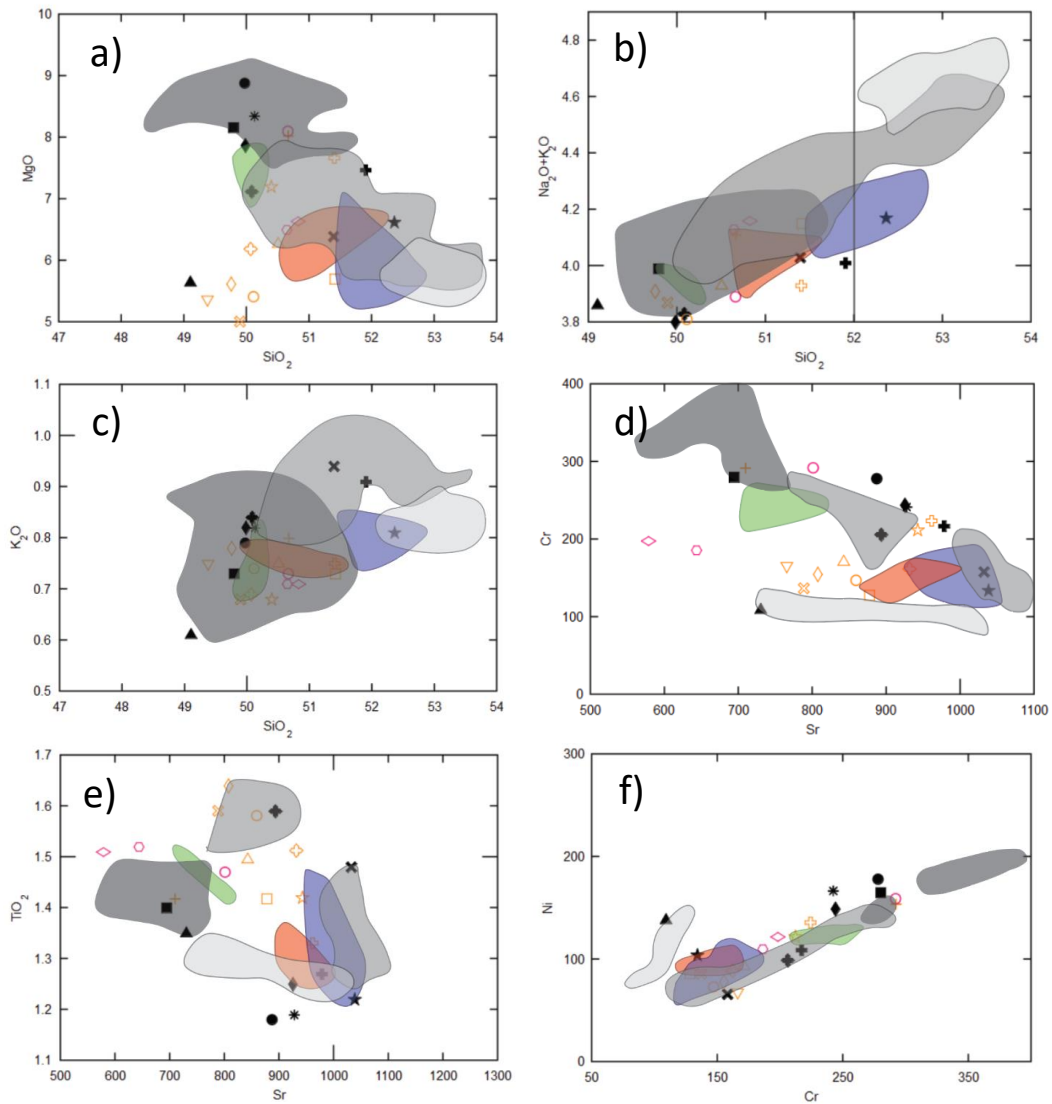


Figure 14. Trench tephra color coded and outlined based on SAHN clusters. SAHN Cluster 1 is green and represents the base of the stratigraphy, SAHN Cluster 2 is blue and represents the lower to middle portion of the stratigraphy, and SAHN Cluster 3 is red and represents the upper portion of the stratigraphy. Major oxide plots a) – c) generally show more mafic and less evolved compositions for SAHN cluster 3 compared to SAHN cluster 2, with lower K₂O and SiO₂, and higher MgO. Trace element compositions d)-e) generally show better agreement with the published lava flow data from Delgine et al. (2016), whereby SAHN cluster 3 plots closer to the Nash group, and SAHN cluster 2 plots well with the Sand group, especially in plot e). SAHN cluster 1 plots along the transition between the Lost Lake and Sand groups. Tephra data from Delgine et al. (2013; orange data points) does not consistently group with any SAHN cluster or lava flow field from the published data.

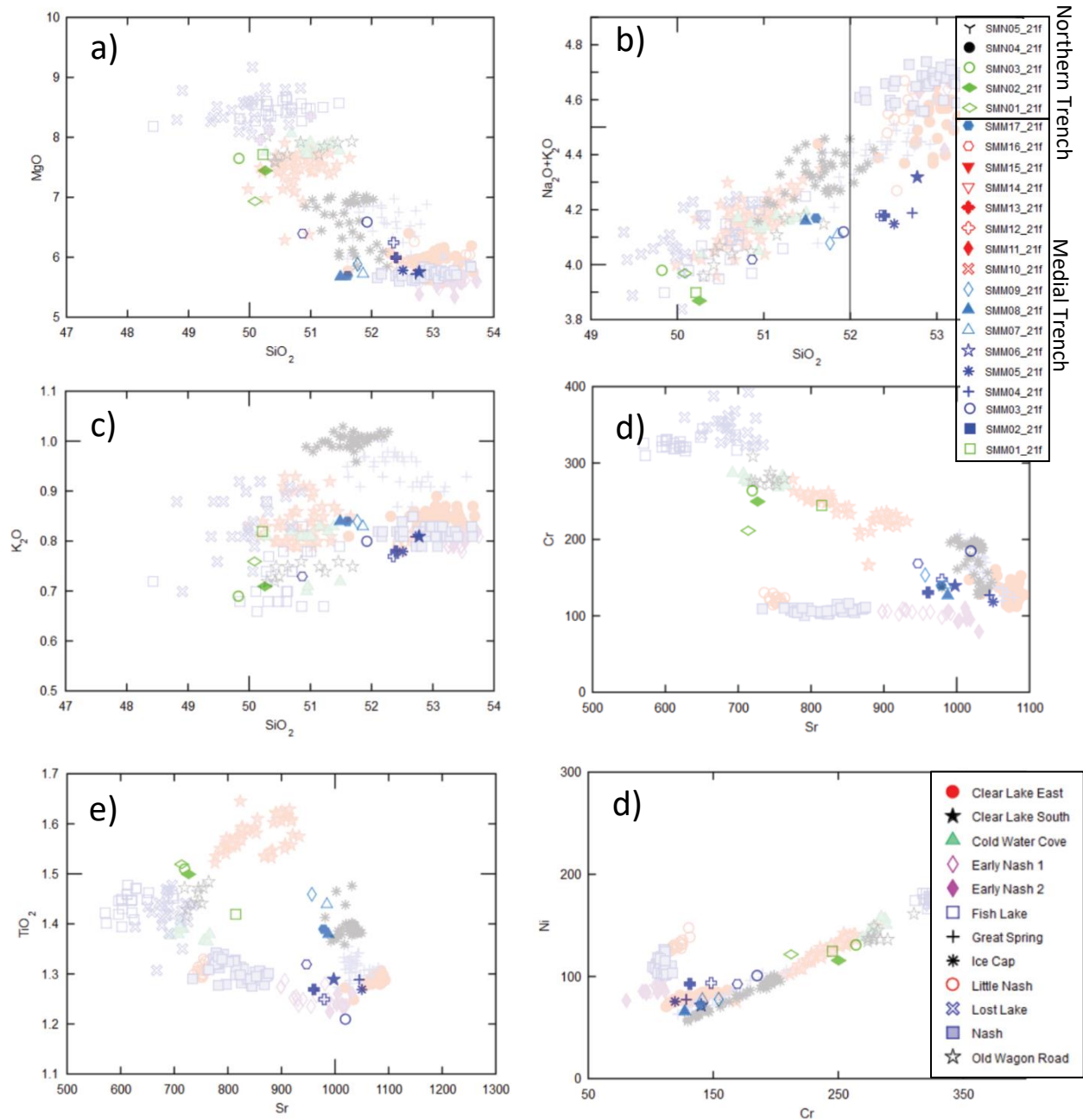


Figure 15. Fourteen tephra samples plotted against the published lava flow subgroups (greyed out to make tephra data more visible) on the same bivariate diagrams presented in figures 9 and 15. Legends for the data and subgroup abbreviations (oldest to youngest from bottom to top) are on the right. Trace element diagrams show more consistent correlation with published subgroups than the major element data and serve as the focus of correlations. For the medial trench, SMM01_21f plots with CLS, SMM03_21f plots with IC, GS and CLE, SMM04_21f and SMM05_21f plot with CLE, and SMM07_21f, SMM08_21f, SMM09_21f, and SMM17_21f plot with IC, GS, and EN. For the Northern Trench, samples SMN01_21f and SMN02_21f correlate with the Sand and Lost Lake Groups, though their subgroups cannot be determined. Sample SMN03_21f plots with CWC and OWR. For the Southern Trench, SMS01_22s plots with CLS, and SMS02_22s and SMS03_22s plot with or near EN I and ENII of the Nash Group, though this is the least well constrained correlation.

Subgroup Abbreviations

- EN II – Early Nash 2
- EN I – Early Nash 1
- CLE – Clear Lake East
- GS – Great Spring
- IC – Ice Cap
- CLS – Clear Lake South
- OWR – Old Wagon Road Canyon
- CWC – Cold Water

Table 3. Listing of all tephra samples, their SAHN Cluster, interpreted geochemical groups (Major Group) and subgroups, and their stratigraphic position in the stratigraphy. See Figure 14 for abbreviations.

Medial Trench							
Sample	SAHN Cluster	Major Group	Subgroup	Stratigraphic Position (cm)		Grain Size	Color
SMM16_21f	3	S/N	-	Top	141-151	fine	brown/black
SMM15_21f	3	S/N	-		131-141	fine	brown/black
SMM14_21f	3	S/N	-		126-131	fine	brown/black
SMM13_21f	3	S/N	-		116-126	fine	black
SMM12_21f	3	S/N	-		106-116	fine	black
SMM11_21f	3	S/N	-		96-106	fine	black
SMM10_21f	3	S/N	-		86-96	medium	black
SMM09_21f	2	S/N	IC, GS or EN		80-86	coarse	black
SMM17_21f	2	S/N	IC, GS or EN		71-102	coarse	black
SMM08_21f	2	S/N	IC, GS or EN		70-80	fine-coarse	black
SMM07_21f	2	S/N	IC, GS or EN		60-70	coarse	black
SMM06_21f	2	S	-		50-60	fine	brown
SMM05_21f	2	S	CLE		40-50	fine	brown/black
SMM04_21f	2	S	CLE		30-40	fine	brown
SMM03_21f	2	S	IC, GS, or CLE		20-30	coarse	black
SMM02_21f	2	S	-		20-Oct	medium	black
SMM01_21f	1	S	CIS	Base	1-10	fine	black
Northern Trench							
SMN05_21f	-	-	-	Top	41-45	fine	brown
SMN04_21f	-	-	-		35-41	coarse	black
SMN03_21f	1	LL	CWC or OWR		25-35	coarse	black
SMN02_21f	1	LL or S	-		15-25	coarse	black
SMN01_21f	1	LL or S	-	Base	5-15	fine	black
Southern Trench							
SMS07_22s	2	S	-	Top	86	fine	black
SMS06_22s	3	S/N	-		80	coarse	black
SMS05_22s	2	S	-		70	fine	black
SMS04_22s	2	S	-		55	fine	black
SMS03_22s	2	N?	EN 1 or 2?		40	medium	black
SMS02_22s	2	N?	EN 1 or 2?		30	fine	black
SMS01_22s	2	S	CLS	Base	15	fine	black
Proximal Trench							
SMP08_21f	-	-	-		76-85 cm	-	-
SMP07_21f	-	-	-		67-76 cm	-	-

Figure 16a shows relative proportions of the elements in Eq. 1 plotted against each other on a ternary diagram. The tephra plots with the published data from Deligne et al. (2016) and there is a slight trend toward CaO and Na₂O loss, which is expected for mafic rocks. When relative proportions of the elements in equation 2 are plotted in similar ternary diagrams (Figure 16b-c), the tephra group plots with the published data, showing only a slight MgO loss

trend. The trend toward Al_2O_3 in Figure 16c and the less pronounced trend in Figure 16a together indicate that MgO experienced the most significant loss during chemical alteration. Thus, the tephra do not exhibit different alteration trends than the lava flows, and probably did not experience enough chemical alteration to contribute significantly to data scattering. Interestingly, when the northern and medial trench CIA and MIA values are plotted against stratigraphic position (Figure 16d-e), SAHN clusters 2 and 3 exhibit distinct trends of increasing CIA and MIA numbers upwards thorough the stratigraphy. This likely indicates a gap in time between the two eruptions that deposited both clusters. SAHN cluster 1 exhibits the least weathering, which, along with a general increase in weathering through the entire trench stratigraphy from bottom to top, makes sense as CIA is known to increase toward the surface (Babechuck et al., 2014), though it must be noted that elements defining CIA and MIA are also influenced by their magmatic concentrations.

Additionally, Figure 17 plots LOI% vs. stratigraphic position and CIA for tephra samples collected in this study, and LOI% vs. CIA for all cone rim samples collected in this study. Generally, no clear trends are seen between CIA and LOI% in the trench tephra or the cone rim scoria, except for sample NC01_21f collected from Nash Crater, which has both a higher CIA and higher LOI%, suggesting the anomalous plotting of that sample on geochemical diagrams may in part result from higher oxidation/alteration compared to all other samples. Indeed, this sample appears to plot slightly off trend from the rest of the collected samples in Figure 15a-c, in agreement with Figure 16. Sample SMM01_21f has an LOI% of -0.04, indicating error during weighing or heating stages. Regardless, this sample still plots well in SAHN Cluster

1, which is expected considering that it was collected at the base of the Medial Trench stratigraphy and thus is still interpretable.

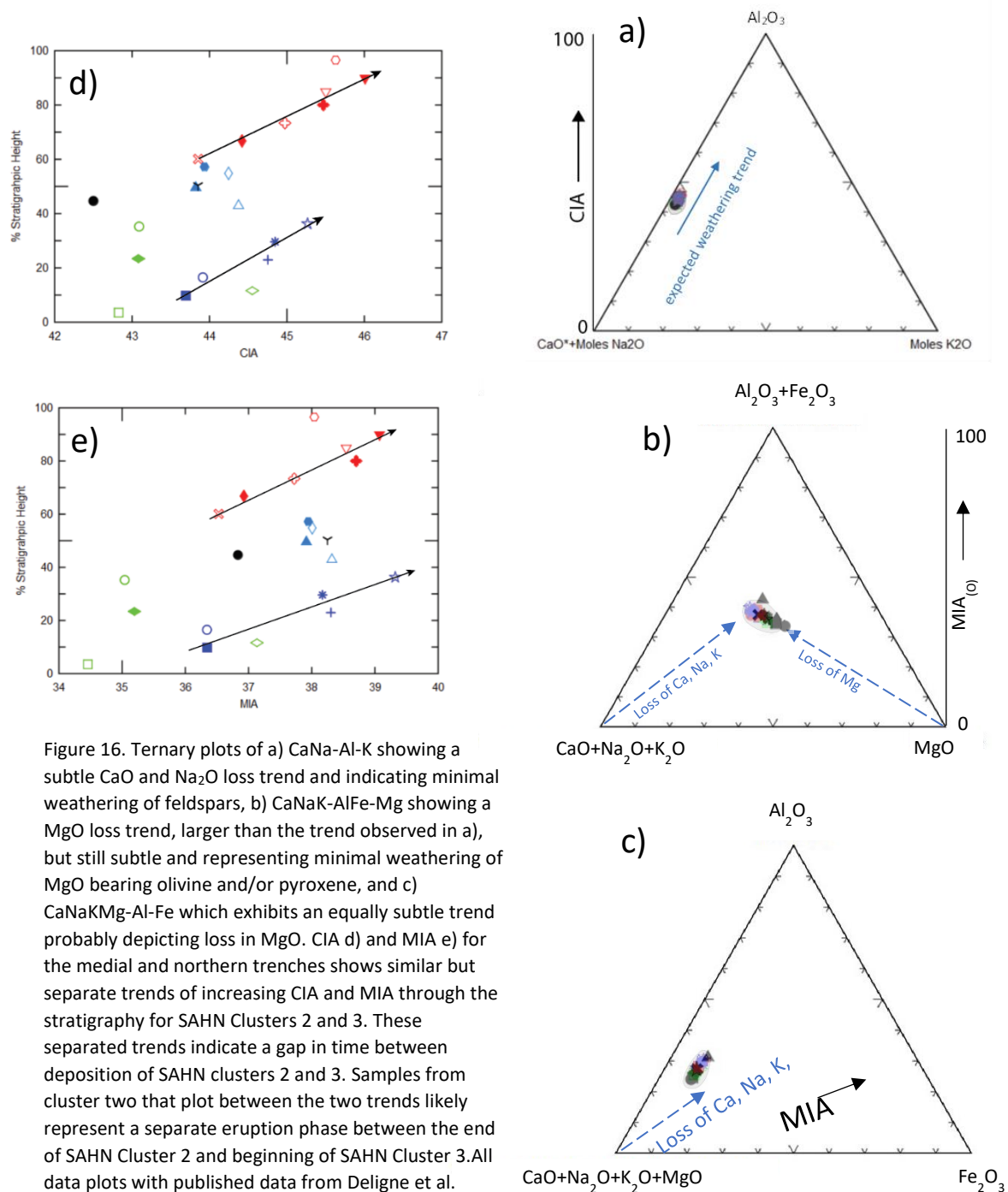


Figure 16. Ternary plots of a) CaNa-Al-K showing a subtle CaO and Na₂O loss trend and indicating minimal weathering of feldspars, b) CaNaK-AlFe-Mg showing a MgO loss trend, larger than the trend observed in a), but still subtle and representing minimal weathering of MgO bearing olivine and/or pyroxene, and c) CaNaKMg-Al-Fe which exhibits an equally subtle trend probably depicting loss in MgO. CIA d) and MIA e) for the medial and northern trenches shows similar but separate trends of increasing CIA and MIA through the stratigraphy for SAHN Clusters 2 and 3. These separated trends indicate a gap in time between deposition of SAHN clusters 2 and 3. Samples from cluster two that plot between the two trends likely represent a separate eruption phase between the end of SAHN Cluster 2 and beginning of SAHN Cluster 3. All data plots with published data from Deligne et al. (2016). These diagrams were modified after Bebechuk et al. (2014).

EMP Mineral Chemistry

Table 4 shows average, median, and range values for all olivine and plagioclase mineral chemistry as determined by EMP analysis. Raw mineral chemistry for all samples are in the Appendix. Olivine Forsterite percentages (Fo%) from trench tephra samples range from Fo₂₃ to Fo₈₆ and 85% of the tephra (196 out of 231 analyses) fall between Fo₈₀ and Fo₈₆. Fo% of the scoria cone samples ranges from Fo₁₁ to Fo₈₆ and 83% of cone samples (34 out of 41 analysis) fall between Fo₈₁ and Fo₈₆. As such, two olivine compositional groups are defined: a low Fo% group from Fo₁₁ to Fo₆₆ with a range of 55, and a high Fo% group from Fo₇₇ to Fo₈₆ with a range of 9. The low Fo% group is much more broadly defined and may represent a later crystallization stage or multiple stages while the high Fo% group likely represents the first crystallization stage. As such, the high Fo% group will be the focus of correlations.

When all tephra Fo% data is plotted together, few trends are visible. For example, Figure 18a shows complete overlap between SAHN clusters 2 and 3 on a plot of molar MgO/(molar MgO + molar Fe₂O₃) vs. Fo%. However, when plotting only the Medial Trench data on the same diagram, SAHN cluster 3 generally exhibits a higher Fo% and higher molar MgO concentrations than SAHN cluster 2, except for sample SMM02_21f which has a higher Fo% and molar MgO concentration than all of SAHN cluster 2 and plots near sample SMM01_21f from SAHN cluster 1 (Figure 18b). Additionally, on a diagram of stratigraphic position vs. Fo% (Figure 18c) for the Medial Trench tephra, a general decreasing trend from samples SMM02_21f to SMM08_21f and an increasing trend from samples SMM10_21f to SMM16_21f are visible. Sample SMM04_21f is an exception, as its Fo% content ranges from Fo_{78.2} to Fo_{81.9}, lower than the rest of the Medial trench data and representing the lowest Fo percentages of the high Fo% group. The transition from the decreasing to increasing trends occurs markedly between the

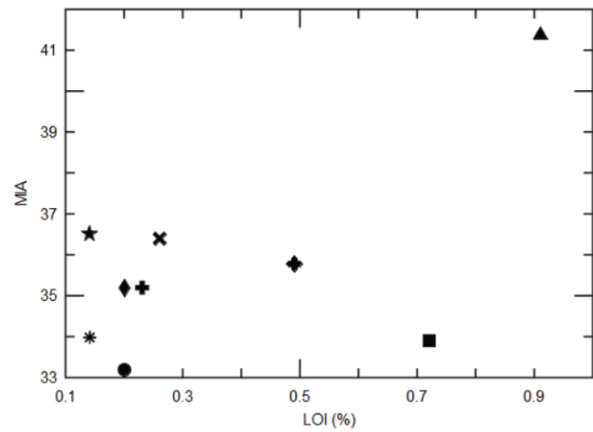
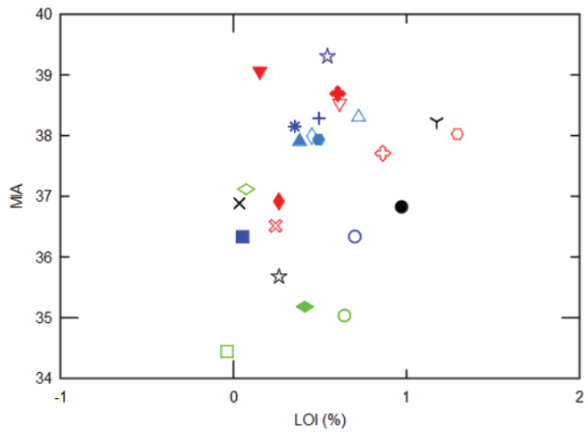
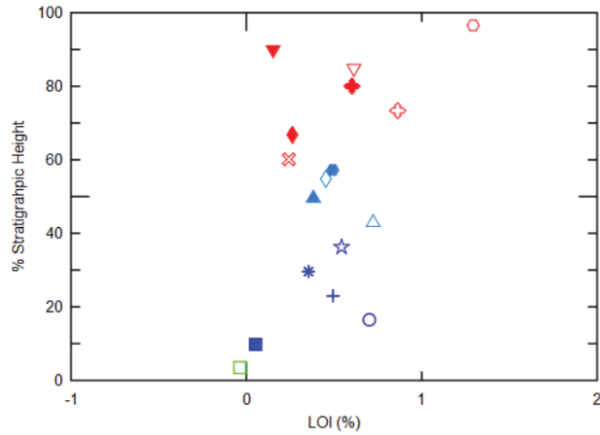


Figure 17. a) LOI% vs. stratigraphic height (measured from bottom up of stratigraphy) and b), LOI% vs. CIA for the SMVF tephra. c) shows LOI% vs. CIA for cone rim samples. Only sample NC01_21f in figure c) (circled in black) shows good agreement between CIA and LOI% with both a higher LOI% and higher CIA number. The rest of the data do not show trends between LOI and CIA and stratigraphic position, indicating variable LOI% does not strongly affect SAHN clusters defined in the tephra geochemical data or the other cone rims sampled in this study.

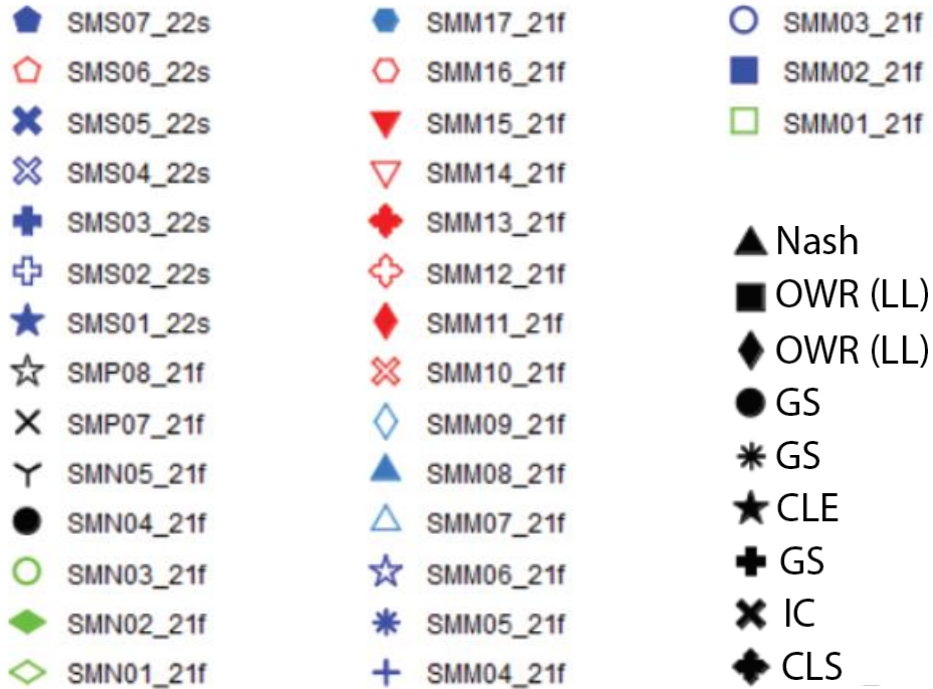
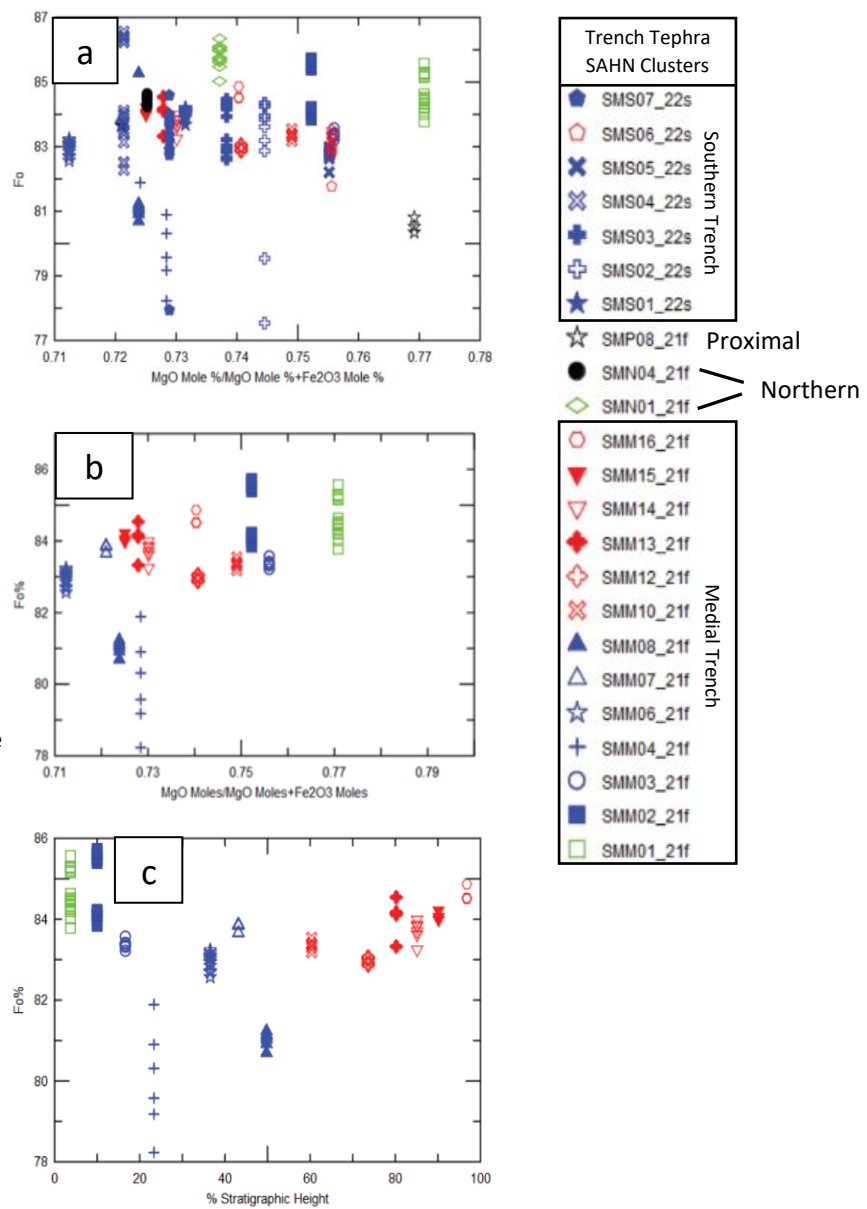


Table 4. EMP data statistics for olivine and plagioclase in Trench Tephra and Cone Rim samples.

Sample Type	Mineral	Fo% Group	Average	Median	Min	Max	Range
Trench Tephra	Olivine	High Fo%	83.6442	83.8164	77.5519	86.5731	9.0212
		Low Fo%	36.23267	33.6896	26.174	66.4391	40.2651
	Plagioclase	N/A	57.17031	58.7919	36.3202	91.7525	55.4323
Scoria Cone	Olivine	High Fo%	84.6347	84.3557	81.2936	86.1945	4.9009
		Low Fo%	40.8723	40.1882	22.7382	48.9144	26.1762
	Plagioclase	N/A	60.37545	58.7234	11.3936	96.7403	85.3467

Figure 18. Plots of MgO mole percentage vs. Fo percentage for a) all analyzed tephra samples and b) medial trench tephra samples. SAHN clusters 2 and 3 overlap significantly in a) but show better separation in b). Plot c) shows a decreasing trend in the stratigraphy for SAHN cluster 2 and an increasing trend for SAHN cluster 3. SAHN cluster 1 is among the highest Fo percentages, as seen across all plots. Green data are SAHN cluster 1, blue data are SAHN cluster 2, and red data are SAHN cluster 3. Black samples don't group well on geochemical diagrams, even when attributed to a SAHN cluster. The samples in each trench progress up through the stratigraphy from bottom to top of the legend on the right.



end of SAHN Cluster 2 and the beginning of SAHN Cluster 3, consistent with the separation between the same two groups seen in the bulk geochemistry.

Trench tephra anorthite percentages (An%) show a relatively continuous grade from An₃₆ to An₆₉ with a range of 33, likely a result of compositional zoning. Thus, determining average anorthite percentage is not reasonable for correlation purposes. This results in difficult delineation of compositional groups within the plagioclase EMP data (Figure 19a). However, when the stratigraphic position is plotted against An% for only the Medial Trench tephra, an increasing trend from An_{54.9} to An_{68.7} in samples SMM11_21f to SMM13_21f and a decreasing trend from An_{68.7} to An_{45.1} in samples SMM13_21f to SMM16_21f is visible in the better grouped lower anorthite percentages for each sample (Figure 19c). Even without ignoring the upper anorthite percentages, sample SMM16_21f, with one analysis returning an An% of An_{61.2}, is the only sample across both trends that doesn't completely agree with the observed trend. If the higher An_{61.8} is ignored, then sample SMM16_21f can also be attributed to the decreasing trend. The cone rim anorthite percentages vary widely with a range of 85.3 from An_{96.7} to An_{11.4} (Figure 19d-e).

Chapter 3: Discussion and Conclusions

Discussion

Geochemical Variation and Data Scattering

Observations that the tephra are largely more mafic and less evolved than the SMVF lava flows follows long established views that basaltic monogenetic cone eruptions generally start with explosive behavior and transition to more effusive behavior (Zawacki et al., 2019). This is due to continued intrusion and eruption of a single magma batch that evolves over time, resulting in more mafic and felsic material being produced in the earlier and later phases of the

eruption cycle respectively. However, like more recent studies have shown (Sun and McDonough, 1989; Morgavi et al., 2017), the geochemistry of volcanic products becomes more complex when petrologic and surficial processes known to influence or constrain geochemical compositions occur, complicating this simplistic view. Though the transition between SAHN Clusters 1 and 2 in the tephra data and the Lost Lake and Sand Groups in the published lava flow data appear to follow this trend, SAHN Cluster 3 in the Tephra data and the Nash Group in

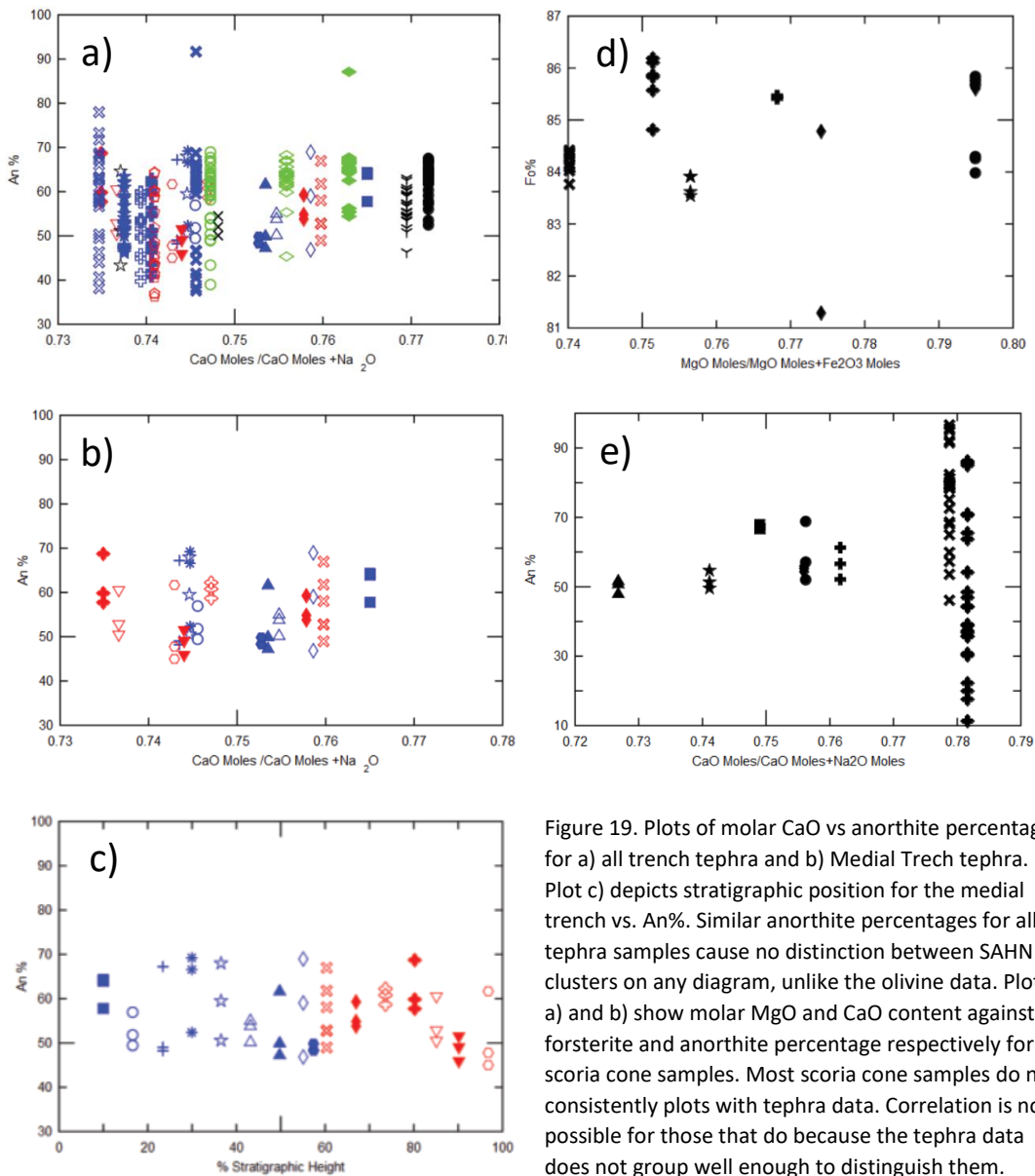


Figure 19. Plots of molar CaO vs anorthite percentage for a) all trench tephra and b) Medial Trench tephra. Plot c) depicts stratigraphic position for the medial trench vs. An%. Similar anorthite percentages for all tephra samples cause no distinction between SAHN clusters on any diagram, unlike the olivine data. Plots a) and b) show molar MgO and CaO content against forsterite and anorthite percentage respectively for scoria cone samples. Most scoria cone samples do not consistently plot with tephra data. Correlation is not possible for those that do because the tephra data does not group well enough to distinguish them.

the published lava flow data do not. As such, these processes, and their possible contribution to variance in the data and discrepancy between data produced in this study and published datasets, are discussed here-in.

In the simplistic view of monogenetic volcanism, fractional crystallization is the dominant process that governs magma differentiation and continued evolution. Fractional crystallization incrementally forms mafic mineral phases that contain MgO, FeO, and CaO as major cations, leaving the residual magma and later erupted products more concentrated in SiO₂, N₂O, and K₂O and producing felsic minerals with those elements as major cations (Sun and McDonough, 1989; Hopkins et al., 2015; Morgavi et al., 2017). Given that SAHN Cluster 3 is more mafic than SAHN Cluster 2, this portion of the stratigraphy does not follow a traditional fractional crystallization trend. A common interpretation of compositional changes from felsic to mafic material is that the volcanic system was recharged with new magma. This interpretation can be applied to the compositional change from the more evolved SAHN Cluster 2 to the less evolved SAHN Cluster 3 seen in the XRF bulk geochemical data and the EMP olivine geochemical data (Figures 14 and 19), particularly for the Medial Trench. Additionally, the change in CIA and MIA numbers between SAHN Clusters 2 and 3 in Figures 16d-e indicate continued deposition through eruption of SAHN Cluster 2, then a gap in time before eruption and deposition of SAHN Cluster 3. However, considering that the elements defining the CIA and MIA equations are also influenced by their magmatic concentrations, then there may not be a significant gap in time between deposition of SAHN Clusters 2 and 3. However, there was likely at least a short gap in time between these two clusters, given that samples SMM07_21f, SMM08_21f, SMM09_21f, and SMM17_21f, all stratigraphically adjacent, group separately

between the rest of SAHN Cluster 2 and SAHN Cluster 3 in Figures 16d-e, indicating a separate eruption event between the two clusters. The length of this time gap is unknown.

Magma mixing also commonly occurs in magmatic systems and can change the elemental composition of the magma to some mixture between the two interacting magmas (Arienzo et al., 2016; Hopkins et al., 2015; Morgavi et al., 2017). This is most easily seen in the EMP mineral chemistry where both olivine and plagioclase data show a range of compositions between forsterite and fayalite, and anorthite and albite. In particular, the high and low Fo% groups from $\sim\text{Fo}_{87}\text{-Fo}_{77}$ and $\text{Fo}_{66}\text{-Fo}_{26}$ indicate two phases of crystal growth: an initial phase in an evolving mafic primary magma, and a second phase when that magma mixed with a more felsic magma, likely left over from a previous recharge event. This is also reflected in the EMP data for the medial trench where the initial samples from SAHN group 3 have forsterite compositions more similar to SAHN group 2, likely a mixture between the more mafic SAHN Cluster 3 recharged magma and SAHN Cluster 2 residual magma, but becomes increasingly mafic towards the top of SAHN Cluster 3 when the residual SAHN Cluster 2 magma has evacuated the magma chamber (samples SMM10_21f to SMM16_21f; Figure 18c). This is important, considering The Nash Group of cones shows evidence for magma recharge in the bulk geochemistry, indicating a possible correlation between SAHN Group 3 and the more mafic portions of the Nash Group (Early Nash 1 and Early Nash 2; Figure 20a-d). This also agrees with figures 14d-e that show trace elements in SAHN Clusters 2 and 3 plotting more closely to the Sand and Nash groups.

Additionally, variability in the geochemical data, particularly in the major elements, may

also reflect heterogeneous growth of microlites in individual tephra. For example, tephra containing abundant plagioclase microlites may have higher concentrations of CaO and Na₂O

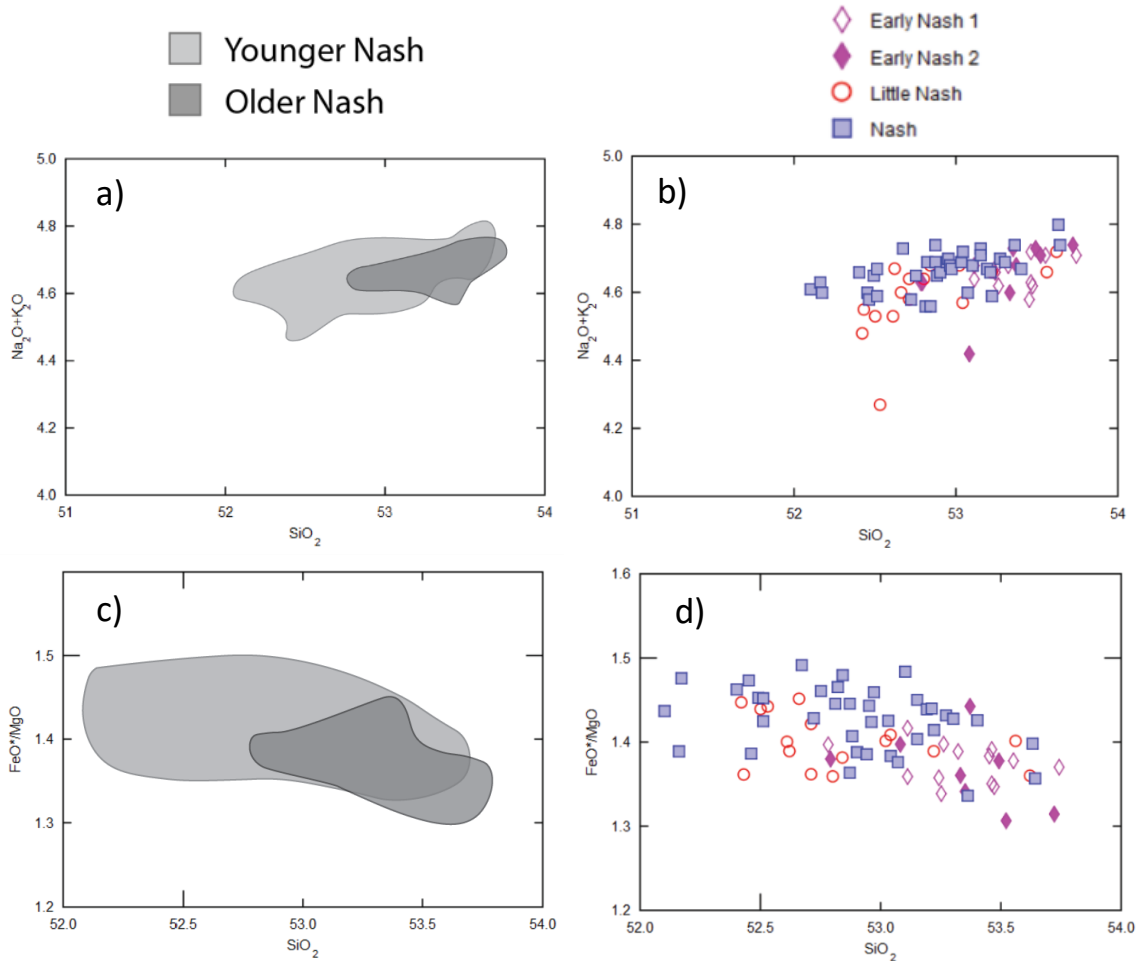


Figure 20. Published Nash Group data from Deligne et al. (2016) showing the younger Nash Group samples as more mafic overall and encompassing a wider range of SiO₂ values in bivariate diagrams of a)-b) SiO₂ vs. Na₂O+K₂O and c)-d) SiO₂ v. FeO*/MgO. This indicates a magma recharge event between deposition of older subgroups Earl Nash 1 and 2 and younger subgroups Little Nash and Nash.

depending on the composition of the plagioclase (Hopkins et al., 2015). The same logic follows for pyroxene with its CaO and FeO end members, and Olivine with its MgO and FeO end members and may explain why the SAHN clusters on the major element plots define a more linear trend in contrast to the trace elements where SAHN Cluster 3 plots off this trend, causing the trace element diagrams to better correlate with the established groups by Deligne et al.

(2016). Stratification of the tephra by density when denser, more crystal-rich tephra fall out of the ash column more proximal to the source vent and less crystal rich ash falling out more distal to the source vent, may provide a mechanism for variable crystal content in the ash. While samples SMN04 and SMN05 from the northern trench, the furthest trench from the chain, do not plot well with the SAHN clusters, samples SMN01_21f through SMN03_21f do plot well and help to define SAHN Cluster 1. This indicates that variation in tephra crystal content and sorting and stratification during fallout do not strongly influence the lower portion of the northern trench or their grouping within SAHN Cluster 1, but may influence upper portions of the stratigraphy.

Crystal content may also partially explain discrepancy in the geochemistry between the scoria cone samples and the tephra samples, as scoria may contain variable plagioclase and other minerals if some of the scoria collected atop the rims were deposited from different eruptions (scoria can fall back into the crater and be included into deposits from later eruptions). Additionally, this discrepancy may also partially be a result of different eruption styles. If the tephra was largely deposited by phreatomagmatic eruptions and the scoria cone was predominantly built by magmatic eruptions, they may show different major and trace element concentrations.

At the surface, climate conditions and vegetation can rework tephra into a mixture between the surface and underlying stratigraphic layers, particularly when tephra layers are thin (Bertrand et al., 2014). This is commonly observed between unconsolidated tephra layers that represent a gap in time and is shown in Appendix A (Figures 23a-b and 24b) where the top portion of the stratigraphy is browner and penetrated by more roots. Additionally, multiple thin

tephra layers may have been collected in individual samples as many were too finely layered to sample directly, also causing potential mixing. However, though some samples collected from layers that are stratigraphically adjacent to each other often cluster together (see sample pairs SMM04_21f and SMM05_21f, SMM07_21f and SMM08_21f in Figure 14 as examples), not all of the pairs are consistently grouped on definable trends within each SAHN Cluster. Further, samples SMM07_21f, SMM08_21f, SMM09_21f, and SMM17_21f, all of which were collected in middle of the Medial Trench and in the upper portion of SAHN Cluster 2, fall between the SAHN Clusters 2 and 3 on figures 16d-e but do not cluster differently than the rest of SAHN Cluster 2 (Figure 21). As such, mixing through reworking and sampling does not appear to significantly affect major geochemical groups defining the three SAHN clusters, but likely does make correlation difficult between the tephra samples and geochemical subgroups defined by Deligne et al. (2016).

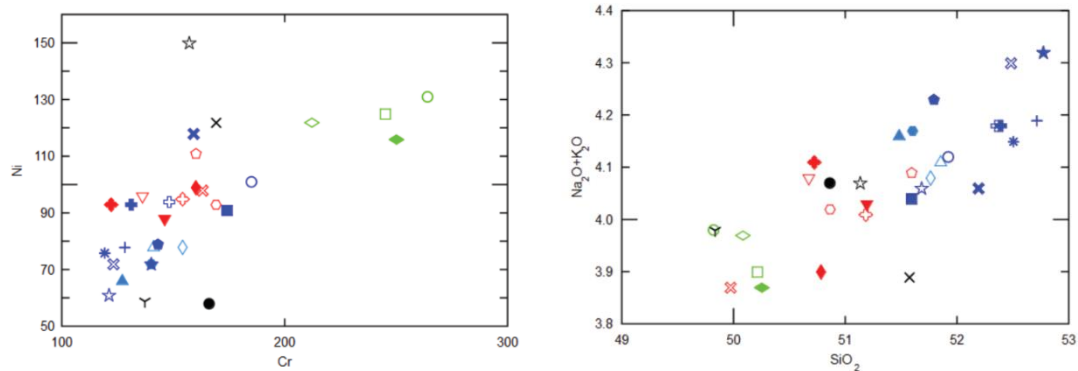


Figure 21. Bivariate geochemical diagrams showing samples SMM07_21f, SMM08_21f, SMM17_21f, and SMM09_21f clustered together at the stratigraphically upper portion of SAHN Cluster 2 in the Medial Trench (color coded light blue) plotting with the rest of SAHN Cluster 2, despite plotting separately in Figure 34d-e, indicating that reworking or mixing did not sufficiently influence the geochemistry of those tephra.

Tephra Correlations and Explosive Eruption Chronology

The three SAHN clusters likely represent the three major geochemical groups defined by Deligne et al. (2016). As such, for the medial Trench, sample SMM01_21f is correlated with the lost lake group or more mafic/earlier lavas of the Sand Group, samples SMM02_21f through SMM09_21f and including SMM17_21f are correlated with the Sand Group and possibly earlier lavas from the Nash Group, and samples SMM10_21f through SMM16_21f are correlated with both the Nash and Sand Groups in agreement with the observation from Deligne et al. (2016) that the Nash and Sand Groups were intermittently active around the same time. For the Northern Trench, samples SMN01_21f through SMN02_21f are correlated with both the Lost Lake and Sand Groups, and sample SMN03_21f is correlated with the Lost Lake Group. Samples SMN04_21f and SMN05_21f do not plot consistently enough to be correlated with any group, though their higher position in the stratigraphy will most likely place them in the Sand and Nash Groups. For the Southern Trench, sample SMS01_22s correlates with the Sand Group and samples SMS02_22s and SMS03_22s correlate with the Nash group. The rest of the southern trench samples did not plot consistently enough to be correlated with a specific group, but most likely correlate with the Sand and/or Nash groups, especially when considering that the basal clay layer was never reached in the Southern Trench, so absence of Lost Lake Group material in the stratigraphy is reasonable. Correlations with specific subgroups are determined in Figure 15 and outlined in table 3.

An eruption chronology for cones that produced portions of the tephra sequence east of the SMVC, not including cones that could not be correlated, from oldest to youngest is as follows: Cold Water Cove and Old Wagon Road of the Lost Lake Group with possible contemporaneous eruption from Clear Lake South of the Sand Group finishing deposition of

SAHN Cluster 1, then either continued eruption from Clear Lake South or beginning eruptions from Ice Cap and Great Spring cones of the Sand Group depositing portions of SAHN Cluster 2, and finally a temporal gap between these eruptions and continued eruption from the Sand and Nash Groups depositing portions of SAHN Group 3, likely contemporaneously and/or intermittently. During this gap in time, a single continuous eruption or multiple temporally linked discrete eruptions deposited samples SMM08_21f, SMM09_21f, and SMN17_21f. Samples SMM07_21f and SMN05_21f have no correlation in the geochemical plots, but may have been erupted together with SMM08_21f and SMM09_21f considering they plot together on figures 16d-e. This would correlate all five samples to the Ice Cap, Great Spring, and/or Early Nash cones, possibly representing the first signature for the Nash Group of cones in the stratigraphy. Figure 22a-b shows stratigraphic columns containing all samples, their interpreted major geochemical group and subgroup correlations, and their SAHN Cluster.

Conclusions

Three major geochemical groups are defined in the SMVF tephra stratigraphy east of the chain of cones and determined by SAHN clustering analysis. These groups are as follows: SAHN Cluster 1 at the base of the stratigraphy, SAHN Cluster 2 in the middle portion of the stratigraphy, and SAHN Cluster 3 in the upper portion of the stratigraphy. These three major geochemical groups generally correlate with the three major geochemical groups defined in the SMVF lava flows by Deligne et al. (2016). As such, SAHN Cluster 1 is generally correlated with the lost Lake Group and more mafic portions of the Sand Group, SAHN Cluster 2 is correlated with the Sand Group and possibly earlier lavas of the Nash Group, and SAHN Cluster 3 is correlated with both the Sand and Nash groups, reflecting explosive activity from both the Sand

Nash groups around the same time. Difficulty in establishing direct correlations between the tephra and the individual cones in the SMVF are likely due to a combination of petrologic processes, including magma recharge, magma mixing, and heterogeneous crystal growth during and prior to eruption, chemical alteration, physical processes including mixing of tephra layers during sample collection and reworking at the surface, density stratification during tephra fallout, re-eruption of scoria initially formed in earlier eruptions and included into deposits of later eruptions, and laboratory error including weighing and heating inconsistencies during sample preparation for X-ray Fluorescence analysis. Regardless of these difficulties, tephra correlations with lava flow geochemical subgroups generally agree with the lava flow stratigraphic and geochemical interpretations from Delinge et al. (2016), with Lost Lake subgroups Cold Water Cove and Old Wagon Road representing the base of the stratigraphy and possibly contemporaneous with Clear Lake South from the Sand Group, and subsequent contemporaneous eruptions from Ice Cap, Great Spring, and Clear Lake East subgroups, and then possible contemporaneous eruptions from Ice Cap and Great Spring, and Early Nash subgroups. This also refutes radiometric ages published in the 1960's that the Lost Lake group of cones is the youngest.

Future work should use machinery to dig larger, better exposed trenches east and west of the SMVF to more easily sample fine layering within the stratigraphy in efforts to mitigate sample mixing during collection. Additional geochemical work should investigate composition of matrix glass in the tephra and cone rim scoria, as these may provide more robust correlations due to matrix glass providing the best representation of the magma composition during eruption and deposition. Considering that trace elemental concentrations more closely

reflect the major geochemical groups in the SMVF lava flows, Inductively Coupled Plasma Mass Spectrometry (ICPMS) should be used to obtain the full suite of trace elements for SMVF tephra and scoria. From this, more geochemical diagrams can be made to more fully characterize the geochemistry and to determine if the observed trends in this study are consistent with other trace elements. This would also help to establish a more detailed petrologic history of the SMVF volcanic products, and could further help correlations. Lastly, Fourier Transform Infrared Spectroscopy (FTIR) analysis should be used to determine water content of the tephra samples which would help to determine if the tephra sequence truly is phreatomagmatic in origin. This would help to further distinguish individual eruptions within the sequence and how they may differentiate from each other, particularly if some of the coarser layers are magmatic in origin. With successful correlation, this could characterize the eruption style for eruptions from individual cones in the chain.

Northern Trench				Southern Trench			
Sample ID	Geochemical Subgroup	Major Geochemical Group	SAHN Cluster	Sample ID	Geochemical Subgroup	Major Geochemical Group	SAHN Cluster
SMN09_21f	Samples not analyzed	Samples not analyzed	Samples not analyzed	SMS07_22s	Unknown	Sand and Nash Groups	SAHN Cluster 3
SMN08_21f							
SMN07_21f							
SMN06_21f							
SMN05_21f	Unknown	Sand and Nash groups?	SAHN Cluster #?	SMS04_22s	CLE/EN	SAHN Cluster 2	
SMN04_21f	CWC or OWR	Lost Lake Group	SAHN Cluster 1	SMS03_22s			
SMN03_21f							
SMN02_21f							
SMN01_21f	Unknown			SMS02_22s			
				SMS01_22s			

Figure 22a. Strat Columns for the Northern and Southern trenches containing all collected samples, their major geochemical groups, and subgroups, and SAHN clusters. See Figure 16 for subgroup abbreviations. The base of stratigraphy is at the bottom and represents the basal clay layer. The dotted line at the base of the Southern Trench represents where sampling started, given that the basal clay layer was not reached for this trench.

Medial Trench			
Sample ID	Geochemical Subgroup	Major Geochemical Group	SAHN Cluster
SMM16_21f	Unknown	Sand and Nash Groups?	SAHN Cluster 3
SMM15_21f			
SMM14_21f			
SMM13_21f			
SMM12_21f			
SMM11_21f			
SMM10_21f			
SMM09_21f	IC, GS, EN		
SMM08_21f/ SMM17_21f			
SMM-07_21f			
SMM06_21f	Unknown	Sand Group	SAHN Cluster 2
SMM05_21f	CLE		
SMM04_21f			
SMM03_21f	IC, GS, or CLE		
SMM02_21f	Unknown		
SMM01_21f	CLS	Transition between Lost Lake and Sand Groups	SAHN Cluster 1

coarse ash

Figure 22b. Stratigraphic column for the Medial Trench containing all collected samples, their major geochemical groups and subgroups, and SAHN clusters. See Figure 16 for subgroup abbreviations. The base of stratigraphy is at the bottom of the column and represents the basal clay layer.

References

- Arienzo, I., Mazzeo, F.C., Moretti R, Cavallo A, D'Antonio, M., 2016, Open-system magma evolution and fluid transfer at Campi Flegrei caldera (Southern Italy) during the past 5 ka as revealed by geochemical and isotopic data: the archetype of Nisida eruption: *Chemical Geology*, v. 427, p. 109–124.
- Babechuk, M.G., Widdowson. M., Kamber, B.S., 2014, Quantifying chemical weathering intensity and trace element release from two contrasting basalt profiles, Deccan Traps, India: *Chemical Geology*, v. 363, p. 56-75.
- Bertrand, S., Daga, R., Bedert, R., Fontijn, K., 2014, Deposition of the 2011–2012 Cordón Caulle tephra (Chile, 40°S) in lake sediments: Implications for tephrochronology and volcanology: *JGR Earth Surface*, v. 119, p. 2555-2753.
- Büttner, R., Dellino, P., and Zimanowski, B., 1999, Identifying magma-water interaction from the surface features of ash particles: *Nature*, v. 401, p. 688–690.
- Calvari, S., Pinkerton, H., 2001, Birth, growth, and morphologic evolution of the 'Laghetto' cinder cone during the 2001 Etna eruption: *Journal of Volcanology and Geothermal Research*, v. 132, p. 224-239.
- Chatters, R.M., 1968, Washington State University natural radio carbon measurements, I: *Radiocarbon*, v. 10, no. 2, p. 479–498.
- Cole, R.P., White, J.D.L., T. Dürig., Büttner, R., Zimanowski, B., Bowman, M.H., Conway, C.E., Leonard, G.S., Pure, L.R., Townsend, D.B., 2021, Controls on andesitic glaciovolcanism at ice-capped volcanoes from field and experimental studies: *Geology*, v. 49, p. 1069-1073.
- Conner, C.B., Stamatakos, J.A., 2000, Ferril, D.A., Hill, B.E., Ofoegbu, G.I., Conway, F.M., Sagar, B., Trapp, J., Geologic factors controlling patterns of small-volume basaltic volcanism: Application to a volcanic hazards assessment at Yucca Mountain, Nevada: *Journal of Geophysical Research*, v. 105, p. 417-432.
- Conway, F.M., Ferril, D.A., Hall, C.M., Morris, A.P., Stamatakos, J. A., Conner, C.B., Halliday, A.N., Condit, C., 1997, Timing of basaltic volcanism along the Mesa Butte Fault in the San Francisco Volcanic Field, Arizona, from $^{40}\text{Ar}/^{39}\text{Ar}$ dates: Implications for longevity of cinder cone alignments: *Journal of Geophysical Research*, v.. 102, p. 815-824.
- Deligne, N.I., Cashman, K.V., and Roering, J.J., 2013, After the lava flow: The importance of external soil sources for plant colonization of recent lava flows in the central Oregon Cascades, USA: *Geomorphology*, v. 202, p. 15–32.

- Deligne, N.I., Conrey, R.M., Cashman, K.V., Champion, D.E., Amidon, W.H., 2016, Holocene volcanism of the upper McKenzie River catchment, central Oregon Cascades, USA: Geological Society of America Bulletin, v. 128, p. 1618-1635.
- Dubes, R.C., 1998 Cluster analysis and related issues: Handbook of Pattern Recognition and Computer Vision (2nd) Edition, World Scientific Publishing Company, p. 3-32
- Dugmore, A., 1989, Icelandic Volcanic Ash in Scotland: Scottish Geographical Magazine, v. 105, p. 168-172.
- Dzurisin, D., Lisowski, M., Wicks, C.W., 2009, Continuing inflation at Three Sisters volcanic center, central Oregon Cascade Range, USA, from GPS, leveling, and InSAR observation: v. 71, p. 1091-1110.
- Erlund, E.J., Cashman, K.V., Wallace, P.J., Pioli, L., Rosi, M., Johnson, E., Granados, H.D., 2010, Compositional evolution of magma from Parícutin Volcano, Mexico: The tephra record: Journal of Volcanology and Geothermal Research, v. 197, p. 167-187.
- Ginibre, C., Kronz, A., Worner, G., 2002, High-resolution quantitative imaging of plagioclase composition using accumulated backscattered electron images: new constraints on oscillatory zoning: Contributions to Mineralogy and Petrology, v. 142, p. 436-448.
- Hopkins, J.L., Millet, M.A., Timm, C., Wilson, C.J.N., Leonard, G.S., Palin, J.M., Neil, H., Tools and techniques for developing tephra stratigraphies in lake cores: A case study from the basaltic Auckland Volcanic Field, New Zealand
- Houghton, B.F., Gonnermann, H.M., 2008, Basaltic explosive volcanism: Constraints from deposits and models: Chemie der Erde – Geochemistry, v. 68., p. 117-140.
- Huges, S.S., Taylor, E.M., 1986, Geochemistry, pedogenesis, and tectonic implications of central High Cascade mafic platform lavas: Geological Society of America Bulletin, v. 97, p. 1024-1036.
- Hughes, S.S, 1990, Mafic Magmatism and associated Tectonism of the Central High Cascade Range, Oregon: Journal of Geophysical Research, v. 95, p. 19,623-19,638.
- Johnson, E.R., Cashman, K.V., 2020, Understanding the storage conditions and fluctuating eruption style of a young monogenetic volcano: Blue Lake crater (<3 ka), High Cascades, Oregon: Journal of Volcanology and Geothermal Research, v. 408, p. 107103.
- Licciardi, J.M., Kurz, M.D., Clark, P.U., and Brook, E.J., 1999, Calibration of cosmogenic ³He production rates from Holocene lava flows in Oregon, USA, and effects of the Earth's magnetic field: Earth and Planetary Science Letters, v. 172, p. 261–271.

- Lisowski, M., McCaffery, R., Wicks, C.W., Dzurisin, D., 2021, Geodetic Constraints on a 25-year Magmatic Inflation Episode Near Three Sisters, Central Oregon: *Journal of Geophysical Research: Solid Earth*, v. 126, e2021JB022360.
- Lowe, D.J., 2011, Tephrochronology and its application: A review: *Quaternary Geology*, v. 6, p. 107-153. Lowe, D.J., Pearce, N.J.G., Jorgensen, M.A., Kuehn, S.C., Tryon, C.A., Hayward, C.L., 2017, Correlating tephtras and cryptotephtras using glass compositional analyses and numerical and statistical methods: review and evaluation: *Quaternary Science Reviews*, v. 175, p. 1-239.
- Lowe, D.J., Pearce, N.J.G., Jorgensen, M.A., Kuehn, S.C., Tryon, C.A., Hayward, C.L., 2017, Correlating tephtras and cryptotephtras using glass compositional analyses and numerical and statistical methods: review and evaluation: *Quaternary Science Reviews*, v. 175, p. 1-239.
- McKay, D., 2012, Recent mafic eruptions at Newberry Volcano and in the central Oregon Cascades: physical volcanology and implications for hazards [Ph.D dissertation]: University of Oregon, p. 148.
- Morgavi, D., Arienzo, I., Montagna, C., 2017, Perugini, D., Dingwell, D.B., Magma Mixing: History and Dynamics of an Eruption Trigger: *Advances in Volcanology*, p. 123-137.
- Nakamura, K., 1977, Volcanoes as possible indicators of tectonic stress orientation – principle and proposal: *Journal of Volcanology and Geothermal Research*, v. 2, p. 1-16.
- Nesbitt, H.W., Young, G.M., 1982, Early Proterozoic climates and plate motions inferred from major element chemistry of lutites: *Nature*, v. 299, p. 715-717.
- Pitcher, B., Kent, A.J.R., Grunder, A.L., 2021, Tephrochronology of North America's most recent arc-sourced ignimbrite flare-up: The Deschutes Formation of the Central Oregon Cascades: *Journal of Volcanology and Geothermal Research*, v. 412, p. 2-23.
- Ruscitto, D.M., 2011, Magmatic volatile contents and explosive cinder cone eruptions in the High Cascades: Recent volcanism in central Oregon and northern California [Ph.D Dissertation: University of Oregon, 182 p.
- Scott, W.E., Iverson, R.M., Schilling, S.P., Fisher, B.J., 2001, Volcano Hazards in the Three Sisters Region, Oregon: U.S Geological Survey Open-File Report 99-437, 13 p., <http://geopubs.wr.usgs.gov/open-file/of99-437/>
- Settle, M., 1979, The Structure and Emplacement of Cinder Cone Fields: *American Journal of Science*, v. 279, p. 1089-1107.

- Sharrod, D.R., Taylor, E.M., Ferns, M.L., Scott, W.E., Conrey, R.M., Smith, G.A., 2004, Geologic Map of the Bend 30- × 60-Minute Quadrangle, Central Oregon: United States Geological Survey Geologic Investigation Series Map I-2683, scale 1:100,000.
- Shea, T., Houghton, B.F., Gurioli, L., Cashman, K.V., Hammer, J.E., Hobden, B.J., 2010, Textural studies of vesicles in volcanic rocks: An integrated methodology: *Journal of Volcanology and Geothermal Research*, v.190, p. 271-289.
- Smith, G.A., Snee, L.W., Taylor, E.M., 1987, Stratigraphic, sedimentologic, and petrologic record of late Miocene subsidence of the central Oregon High Cascades: *Geology*, v. 15, p. 387-392.
- Smith, G.A., Taylor, E.M., 1983, The Central Oregon High Cascade graben: What? Where? When?: v. 7, p. 275-279
- Sun, W., McDonough, W, 1989, Chemical and isotopic systematics of oceanic basalts: implications for mantle composition and processes: Geological Society, London, Special Publications, v. 42, p. 313-345.
- Taddeucci, J., Pompillio, M., Scarlato, P., 2004, Conduit processes during the July–August 2001 explosive activity of Mt. Etna (Italy): inferences from glass chemistry and crystal size distribution of ash particles: *Journal of Volcanology and Geothermal Research*, v. 137, p. 33-54.
- Tanaka, K.L., Shoemaker, E.M., Ulrich, G.E., Wolfe, E.W., 1986, Migration of volcanism in the San Francisco volcanic field, Arizona: *Geological Society of America Bulletin*, v. 97, p. 129-141.
- Taylor, E.M., 1965, Recent volcanism between Three Fingered Jack and North Sister, Oregon Cascade Range: Part I—History of volcanic activity: *The Ore Bin*, v. 27, p. 121-147.
- 1968, Roadside geology, Santiam and McKenzie Pass high ways, Oregon, in Dole, H.M., ed., *Andesite Conference Guide book*: Oregon Department of Geology and Mineral Industries Bulletin 62, p. 3-34.
- 1978. Field geology of SW Broken Top quadrangle, Oregon v. 2, State of Oregon, Department of Geology and Mineral Industries, 50 p.
- 1990, Sand Mountain, Oregon, and Belknap, Oregon, *in* Wood, C.A., and Kienle, Jürgen, eds., *Volcanoes of North America (United States and Canada)*: Cambridge, Cambridge University Press, p. 180-183.

- Valentine, G., Krier, D.J., Perry, F.V., Heiken, G., 2007, Eruptive and geomorphic processes at the Lathrop Wells scoria cone volcano: *Journal of Volcanology and Geothermal Research*, v. 161, p. 57-80.
- Wells, R.E., McCaffrey, R., 2013, Steady rotation of the Cascade arc: *Geology*, v. 41, p. 1027-1030.
- White, J.D.L., Valentine, G.A., 2016, Magmatic versus phreatomagmatic fragmentation: Absence of evidence is not evidence of absence: *Geosphere*, v. 12, p. 1478-1488.
- Wicks, C.W., Dzurisin, D., Ingebritsen, S., Thatcher, W., Lu, Z., Iverson, J., 2002, Magmatic activity beneath the quiescent Three Sisters volcanic center, central Oregon Cascade Range, USA: *Geophysical Research Letters*, v. 29, p. 26-1-26-4.
- Zawacki, E.E., Clarke, A.B., Arrowsmith, J.R., Bonadonna, C., Lynch, D.J., Tecolote volcano, Pinacate volcanic field (Sonora, Mexico): A case of highly explosive basaltic volcanism and shifting eruptive styles: *Journal of Volcanology and Geothermal Research*, v. 379, p. 23-44.

Appendix A: Trench Photos



Figure 23. photos of the Medial Trench. photo c) shows massive fine tephra which typifies the SMVF tephra when fine layering is absent.





Figure 24. Northern trench digging and sampling. The brown/orange material at the bottom of photo c) is the basal clay layer. This trench was also the furthest away from the SMVF chain of cones and was the most vegetated of all the trenches.





Figure 25. Southern trench digging and sampling. The brown material seen at the surface and in the upper layers in photos a) and b) is the surficial reworked material, and photo c) provides an example of typical fine layering in the SMVF.





Figure 26. Proximal trench digging and sampling. Sand Mountain North is in the background of photo a), roots are visible in the upper portion of the trench in photo b), and the bottom half of the stratigraphy in photo c) shows slightly coarser layering compared to Figure 23c, while the upper half shows massive tephra similar to Figure 21c.



Appendix B: Tephra Geochemistry

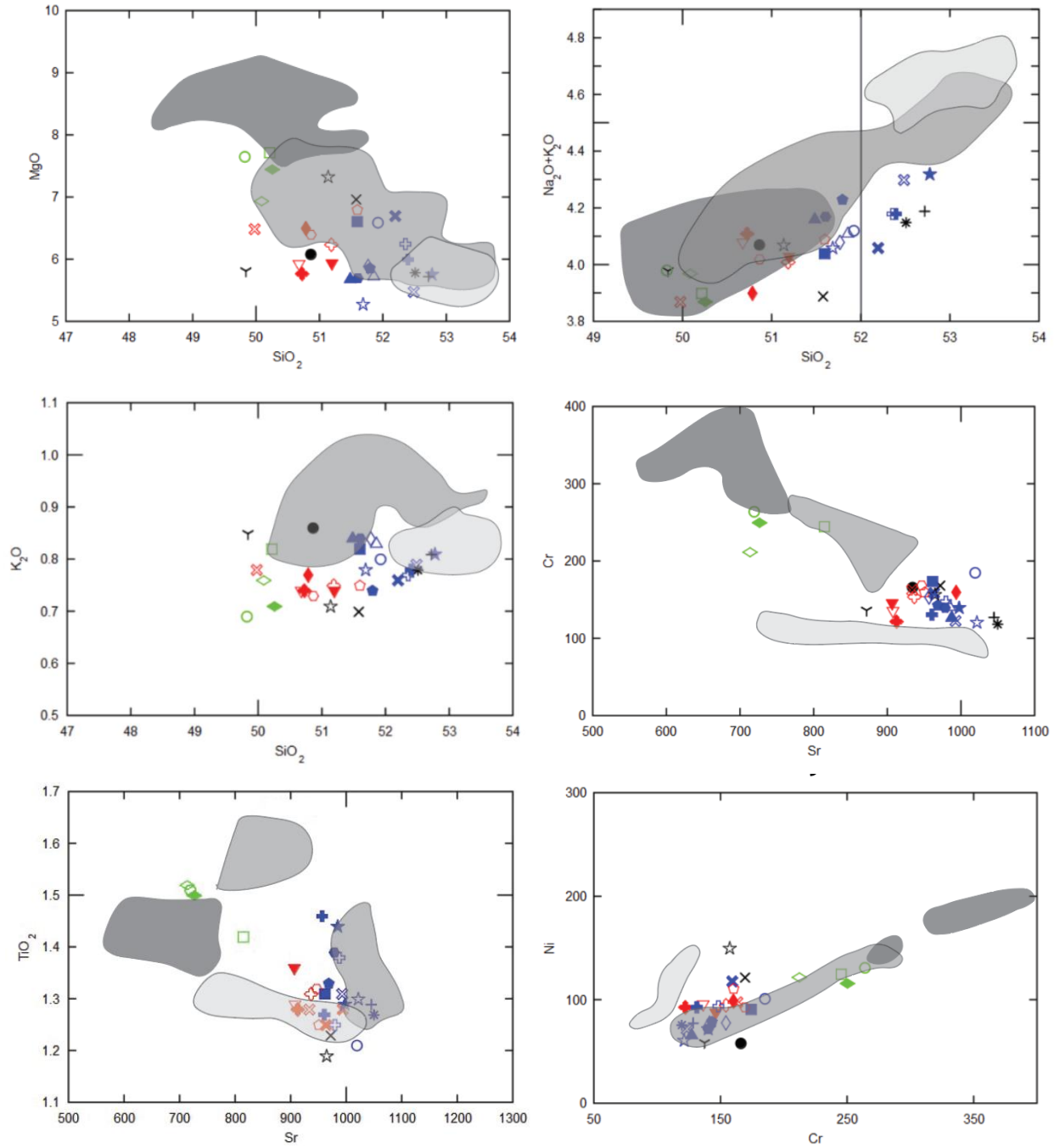


Figure 27. Plots from figure 13a-f, but with no fields drawn around the SAHN groups, showing their clustering.

Appendix C: EMP Mineral Chemistry Tables

Table 5. Olivine forsterite percentage for all analyzed samples. Crystal grains were analyzed each sample were analyzed multiple times, and individual grains are notated by the number at the end of sample names.

SAMPLE	Fo%				
SM03_ol	39.68	SM19_22S_ol_2	86.11	SMM04_21f_ol_1	79.19
SM03_ol	81.29	SM19_22S_ol_2	86.19	SMM04_21f_ol_1	79.59
SM03_ol	84.79	SMM01_21f_ol_1	83.79	SMM04_21f_ol_1	80.33
SM04_22S_ol	85.61	SMM01_21f_ol_1	84.03	SMM04_21f_ol_1	80.92
SM04_22S_ol	85.68	SMM01_21f_ol_1	84.21	SMM04_21f_ol_1	81.91
SM04_22S_ol	85.77	SMM01_21f_ol_1	84.25	SMM06_21f_ol_1	82.73
SM04_22S_ol	85.84	SMM01_21f_ol_1	84.34	SMM06_21f_ol_1	82.95
SM04_22S_ol2	83.99	SMM01_21f_ol_1	84.35	SMM06_21f_ol_1	82.95
SM04_22S_ol2	84.26	SMM01_21f_ol_1	84.43	SMM06_21f_ol_1	83.08
SM04_22S_ol2	84.30	SMM01_21f_ol_1	84.46	SMM06_21f_ol_1	83.13
SM06_ol	22.74	SMM01_21f_ol_1	84.47	SMM06_21f_ol_1	83.25
SM06_ol	37.29	SMM01_21f_ol_1	84.52	SMM06_21f_ol_2	82.59
SM06_ol	40.19	SMM01_21f_ol_1	84.53	SMM06_21f_ol_2	82.70
SM06_ol	83.55	SMM01_21f_ol_1	84.64	SMM06_21f_ol_2	82.86
SM06_ol	83.63	SMM01_21f_ol_2	85.17	SMM06_21f_ol_2	82.96
SM06_ol	83.92	SMM01_21f_ol_2	85.21	SMM06_21f_ol_2	83.03
SM06_ol	83.93	SMM01_21f_ol_2	85.27	SMM06_21f_ol_2	83.20
SM06_ol	83.93	SMM01_21f_ol_2	85.30	SMM07_21f_ol_1	83.66
SM07_22S_ol	48.54	SMM01_21f_ol_2	85.30	SMM07_21f_ol_1	83.68
SM07_22S_ol	48.76	SMM01_21f_ol_2	85.58	SMM07_21f_ol_1	83.85
SM07_22S_ol	48.91	SMM02_21f_ol_1	85.40	SMM07_21f_ol_1	83.87
SM07_22S_ol2	85.42	SMM02_21f_ol_1	85.48	SMM07_21f_ol_1	83.88
SM07_22S_ol2	85.45	SMM02_21f_ol_1	85.51	SMM07_21f_ol_1	83.88
SM07_22S_ol2	85.48	SMM02_21f_ol_1	85.64	SMM08_21f_ol	85.28
SM18_22S_ol_1	84.10	SMM02_21f_ol_1	85.66	SMM08_21f_ol_1	81.15
SM18_22S_ol_2	83.77	SMM02_21f_ol_1	85.75	SMM08_21f_ol_2	81.24
SM18_22S_ol_2	84.10	SMM02_21f_ol_2	83.84	SMM08_21f_ol_3	81.11
SM18_22S_ol_3	84.03	SMM02_21f_ol_2	83.99	SMM08_21f_ol_4	80.70
SM18_22S_ol_3	84.43	SMM02_21f_ol_2	84.09	SMM08_21f_ol_5	80.93
SM18_22S_ol_4	84.14	SMM02_21f_ol_2	84.13	SMM08_21f_ol_6	81.04
SM18_22S_ol_4	84.37	SMM02_21f_ol_2	84.18	SMM08_21f_ol2	34.94
SM18_22S_ol_5	84.17	SMM02_21f_ol_2	84.24	SMM08_21f_ol2	39.22
SM18_22S_ol_5	84.39	SMM03_21f_ol_2	83.22	SMM10_21f_ol_1	66.44
SM18_22S_ol_6	84.29	SMM03_21f_ol_2	83.32	SMM10_21f_ol_1	83.20
SM18_22S_ol_6	84.34	SMM03_21f_ol_2	83.35	SMM10_21f_ol_1	83.31
SM18_22S_ol_7	84.14	SMM03_21f_ol_2	83.40	SMM10_21f_ol_1	83.38
SM19_22S_ol_2	84.82	SMM03_21f_ol_2	83.42	SMM10_21f_ol_1	83.41
SM19_22S_ol_2	85.58	SMM03_21f_ol_2	83.58	SMM10_21f_ol_1	83.55
SM19_22S_ol_2	85.83	SMM04_21f_ol	83.67	SMM12_21f_ol	33.69
SM19_22S_ol_2	85.87	SMM04_21f_ol_1	78.25	SMM12_21f_ol	36.02

Table 5 continued.

SMM12_21f_ol	42.49	SMN04_21f_ol_1	84.25	SMS02_22S_ol_2	29.30
SMM12_21f_ol_1	82.87	SMN04_21f_ol_1	84.34	SMS02_22S_ol_2	30.13
SMM12_21f_ol_1	82.90	SMN04_21f_ol_1	84.45	SMS02_22S_ol_2	30.96
SMM12_21f_ol_1	82.94	SMN04_21f_ol_1	84.53	SMS02_22S_ol_2	31.53
SMM12_21f_ol_1	83.02	SMN04_21f_ol_1	84.58	SMS02_22S_ol_2	31.90
SMM12_21f_ol_1	83.06	SMN04_21f_ol_1	84.64	SMS02_22S_ol_2	32.52
SMM12_21f_ol_1	83.09	SMP07_ol	50.81	SMS02_22S_ol_2	32.83
SMM13_21f_ol	83.34	SMP07_ol	51.31	SMS02_22S_ol_2	34.49
SMM13_21f_ol2	84.12	SMP07_ol	51.69	SMS02_22S_ol_2	34.60
SMM13_21f_ol2	84.18	SMP07_ol2	31.70	SMS02_22S_ol_2	35.10
SMM13_21f_ol2	84.55	SMP07_ol2	41.00	SMS02_22S_ol_2	37.58
SMM14_21f_ol_1	83.26	SMP07_ol2	41.17	SMS03_22S_ol_1	82.62
SMM14_21f_ol_1	83.63	SMP08_22S_ol	80.37	SMS03_22S_ol_1	82.66
SMM14_21f_ol_1	83.72	SMP08_22S_ol	80.54	SMS03_22S_ol_1	82.85
SMM14_21f_ol_1	83.84	SMP08_22S_ol	80.83	SMS03_22S_ol_1	82.91
SMM14_21f_ol_1	83.87	SMS01_22S_ol_1	83.70	SMS03_22S_ol_1	83.04
SMM14_21f_ol_1	84.00	SMS01_22S_ol_1	83.90	SMS03_22S_ol_1	83.23
SMM15_ol	84.00	SMS01_22S_ol_1	83.96	SMS03_22S_ol_2	83.94
SMM15_ol	84.07	SMS01_22S_ol_1	84.01	SMS03_22S_ol_2	84.18
SMM15_ol	84.23	SMS01_22S_ol_1	84.05	SMS03_22S_ol_2	84.25
SMM15_ol2	26.17	SMS01_22S_ol_1	84.06	SMS03_22S_ol_2	84.29
SMM15_ol2	26.66	SMS01_22S_ol_1	84.07	SMS03_22S_ol_2	84.39
SMM15_ol2	27.37	SMS01_22S_ol_1	84.11	SMS03_22S_ol_2	84.48
SMM16_ol	84.52	SMS01_22S_ol_1	84.13	SMS04_22S_ol_1	82.30
SMM16_ol	84.54	SMS01_22S_ol_1	84.16	SMS04_22S_ol_1	82.52
SMM16_ol	84.88	SMS01_22S_ol_1	84.21	SMS04_22S_ol_1	83.45
SMM17_ol	30.13	SMS01_22S_ol_1	84.21	SMS04_22S_ol_1	83.54
SMM17_ol	31.15	SMS02_22S_ol_1	77.55	SMS04_22S_ol_1	83.76
SMN01_21f_ol_1	85.99	SMS02_22S_ol_1	79.56	SMS04_22S_ol_1	84.00
SMN01_21f_ol_1	86.01	SMS02_22S_ol_1	82.88	SMS04_22S_ol_1	84.03
SMN01_21f_ol_1	86.02	SMS02_22S_ol_1	83.20	SMS04_22S_ol_1	84.13
SMN01_21f_ol_1	86.09	SMS02_22S_ol_1	83.63	SMS04_22S_ol_2	82.53
SMN01_21f_ol_1	86.11	SMS02_22S_ol_1	83.86	SMS04_22S_ol_2	83.15
SMN01_21f_ol_1	86.36	SMS02_22S_ol_1	83.96	SMS04_22S_ol_2	83.44
SMN01_21f_ol_2	85.04	SMS02_22S_ol_1	83.96	SMS04_22S_ol_2	83.69
SMN01_21f_ol_2	85.49	SMS02_22S_ol_1	84.27	SMS04_22S_ol_2	83.75
SMN01_21f_ol_2	85.63	SMS02_22S_ol_1	84.28	SMS04_22S_ol_2	84.01
SMN01_21f_ol_2	85.69	SMS02_22S_ol_1	84.35	SMS04_22S_ol_3	86.25
SMN01_21f_ol_2	85.74	SMS02_22S_ol_1	84.36	SMS04_22S_ol_3	86.28
SMN01_21f_ol_2	85.76	SMS02_22S_ol_2	27.86	SMS04_22S_ol_3	86.37

Table 5 continued.

SMS04_22S_ol_3	86.43	SMS06_22S_ol_1	82.99	SMS07_22S_ol_1	83.66
SMS04_22S_ol_3	86.44	SMS06_22S_ol_1	83.00	SMS07_22S_ol_1	83.77
SMS04_22S_ol_3	86.57	SMS06_22S_ol_1	83.04	SMS07_22S_ol_1	83.88
SMS05_22S_ol_1	82.22	SMS06_22S_ol_1	83.40	SMS07_22S_ol_1	84.01
SMS05_22S_ol_1	82.65	SMS06_22S_ol_2	81.79	SMS07_22S_ol_1	84.61
SMS05_22S_ol_1	82.74	SMS06_22S_ol_2	82.79	SMS07_22S_ol_2	82.76
SMS05_22S_ol_1	82.82	SMS06_22S_ol_2	83.23	SMS07_22S_ol_2	82.90
SMS05_22S_ol_1	82.90	SMS06_22S_ol_2	83.38	SMS07_22S_ol_2	82.94
SMS05_22S_ol_1	83.00	SMS06_22S_ol_2	83.38	SMS07_22S_ol_2	82.94
SMS06_22S_ol_1	82.87	SMS06_22S_ol_2	83.54	SMS07_22S_ol_2	83.19
SMS06_22S_ol_1	82.96	SMS07_22S_ol_1	77.96	SMS07_22S_ol_2	83.38

Table 6. Plagioclase anorthite percentage for all analyzed samples. Crystal grains were analyzed each sample were analyzed multiple times, and individual grains are notated by the number at the end of sample names.

SAMPLE	An %				
NC01_22S	47.97	SM18_22S_plg_gl1_g2	79.51	SM19_22S_plg_gl1_g2	63.81
NC01_22S	50.73	SM18_22S_plg_gl1_g2	79.88	SM19_22S_plg_gl2_g1	17.68
NC01_22S	51.69	SM18_22S_plg_gl1_g2	81.43	SM19_22S_plg_gl2_g1	22.33
SM02_22S	66.87	SM18_22S_plg_gl1_g2	82.49	SM19_22S_plg_gl2_g1	30.35
SM02_22S	66.88	SM18_22S_plg_gl2_g1	68.76	SM19_22S_plg_gl2_g1	30.83
SM02_22S	68.03	SM18_22S_plg_gl2_g1	75.24	SM19_22S_plg_gl2_g1	46.98
SM03_22S	54.45	SM18_22S_plg_gl2_g1	78.42	SM19_22S_plg_gl2_g1	85.10
SM03_22S	55.38	SM18_22S_plg_gl2_g1	78.55	SM19_22S_plg_gl2_g2	36.87
SM03_22S	56.03	SM18_22S_plg_gl2_g1	79.06	SM19_22S_plg_gl2_g2	48.55
SM04_22S	52.08	SM18_22S_plg_gl2_g1	79.92	SM19_22S_plg_gl2_g2	54.26
SM04_22S	57.19	SM18_22S_plg_gl2_g2	60.04	SM19_22S_plg_gl2_g2	71.05
SM04_22S	68.88	SM18_22S_plg_gl2_g2	91.63	SM19_22S_plg_gl2_g2	85.73
SM06_22S	49.68	SM18_22S_plg_gl2_g2	92.23	SM19_22S_plg_gl2_g2	86.31
SM06_22S	51.46	SM18_22S_plg_gl2_g2	95.10	SMM02_21F	57.87
SM06_22S	54.81	SM18_22S_plg_gl2_g2	95.73	SMM02_21F	64.03
SM07_22S	52.25	SM18_22S_plg_gl2_g2	96.74	SMM02_21F	64.37
SM07_22S	56.71	SM19_22S_plg_gl1_g1	20.04	SMM03_21F	49.48
SM07_22S	61.44	SM19_22S_plg_gl1_g1	35.76	SMM03_21F	51.85
SM18_22S_plg_gl1_g1	46.21	SM19_22S_plg_gl1_g1	38.89	SMM03_21F	56.98
SM18_22S_plg_gl1_g1	53.67	SM19_22S_plg_gl1_g1	44.48	SMM04_21F	48.35
SM18_22S_plg_gl1_g1	65.11	SM19_22S_plg_gl1_g1	65.60	SMM04_21F	49.19
SM18_22S_plg_gl1_g1	68.12	SM19_22S_plg_gl1_g1	70.72	SMM04_21F	67.36
SM18_22S_plg_gl1_g1	72.70	SM19_22S_plg_gl1_g2	11.39	SMM05_21F	52.51
SM18_22S_plg_gl1_g1	81.32	SM19_22S_plg_gl1_g2	35.90	SMM05_21F	66.68
SM18_22S_plg_gl1_g2	57.40	SM19_22S_plg_gl1_g2	37.42	SMM05_21F	69.36
SM18_22S_plg_gl1_g2	79.39	SM19_22S_plg_gl1_g2	39.23	SMM06_21F	50.66
		SM19_22S_plg_gl1_g2	44.29	SMM06_21F	59.59

Table 6 continued.

SMM06_21F	68.09	SMN01_21f_plg_gl1_g1	64.23	SMN02_21f_plg_gl2_g2	56.25
SMM07_21F	50.25	SMN01_21f_plg_gl1_g1	64.73	SMN02_21f_plg_gl2_g2	56.35
SMM07_21F	53.88	SMN01_21f_plg_gl1_g2	62.90	SMN02_21f_plg_gl2_g2	87.20
SMM07_21F	55.09	SMN01_21f_plg_gl1_g2	63.51	SMN03_21f_plg_gl1_g1	59.10
SMM08_21F	47.28	SMN01_21f_plg_gl1_g2	63.62	SMN03_21f_plg_gl1_g1	60.37
SMM08_21F	49.94	SMN01_21f_plg_gl1_g2	63.88	SMN03_21f_plg_gl1_g1	62.40
SMM08_21F	61.67	SMN01_21f_plg_gl1_g2	64.57	SMN03_21f_plg_gl1_g1	63.09
SMM09_21F	46.94	SMN01_21f_plg_gl1_g2	68.38	SMN03_21f_plg_gl1_g1	63.21
SMM09_21F	59.14	SMN01_21f_plg_gl2_g1	63.47	SMN03_21f_plg_gl1_g1	63.49
SMM09_21F	69.06	SMN01_21f_plg_gl2_g1	64.14	SMN03_21f_plg_gl2_g1	49.15
SMM10_21F	49.08	SMN01_21f_plg_gl2_g1	64.22	SMN03_21f_plg_gl2_g1	50.43
SMM10_21F	52.81	SMN01_21f_plg_gl2_g1	65.72	SMN03_21f_plg_gl2_g1	52.52
SMM10_21F	52.94	SMN01_21f_plg_gl2_g1	66.91	SMN03_21f_plg_gl2_g1	54.02
SMM10_21F	58.14	SMN01_21f_plg_gl2_g1	67.20	SMN03_21f_plg_gl2_g1	54.03
SMM10_21F	61.89	SMN01_21f_plg_gl2_g2	45.44	SMN03_21f_plg_gl2_g1	54.09
SMM10_21F	67.07	SMN01_21f_plg_gl2_g2	55.44	SMN03_21f_plg_gl2_g2	59.92
SMM11_21F	53.89	SMN01_21f_plg_gl2_g2	59.98	SMN03_21f_plg_gl2_g2	62.47
SMM11_21F	54.91	SMN01_21f_plg_gl2_g2	61.27	SMN03_21f_plg_gl2_g2	63.24
SMM11_21F	59.34	SMN01_21f_plg_gl2_g2	61.99	SMN03_21f_plg_gl2_g2	63.95
SMM12_21F	58.77	SMN01_21f_plg_gl2_g2	62.30	SMN03_21f_plg_gl2_g2	64.31
SMM12_21F	60.89	SMN02_21f_plg_gl1_g1	65.25	SMN03_21f_plg_gl2_g2	65.27
SMM12_21F	62.33	SMN02_21f_plg_gl1_g1	66.93	SMN03_21f_plg_gl3_g1	43.43
SMM13_21F	57.81	SMN02_21f_plg_gl1_g1	67.10	SMN03_21f_plg_gl3_g1	61.24
SMM13_21F	59.92	SMN02_21f_plg_gl1_g1	67.40	SMN03_21f_plg_gl3_g1	66.55
SMM13_21F	68.80	SMN02_21f_plg_gl1_g1	67.77	SMN03_21f_plg_gl3_g1	67.01
SMM14_21F	50.59	SMN02_21f_plg_gl1_g1	67.83	SMN03_21f_plg_gl3_g1	67.75
SMM14_21F	52.97	SMN02_21f_plg_gl1_g2	64.83	SMN03_21f_plg_gl3_g1	69.01
SMM14_21F	60.66	SMN02_21f_plg_gl1_g2	65.57	SMN03_21f_plg_gl3_g2	39.03
SMM15_22S	46.01	SMN02_21f_plg_gl1_g2	66.31	SMN03_21f_plg_gl3_g2	48.96
SMM15_22S	49.15	SMN02_21f_plg_gl1_g2	66.68	SMN03_21f_plg_gl3_g2	58.18
SMM15_22S	51.63	SMN02_21f_plg_gl1_g2	66.74	SMN03_21f_plg_gl3_g2	59.45
SMM16_22S	45.10	SMN02_21f_plg_gl1_g2	66.85	SMN03_21f_plg_gl3_g2	61.60
SMM16_22S	47.86	SMN02_21f_plg_gl2_g1	62.58	SMN03_21f_plg_gl3_g2	63.86
SMM16_22S	61.78	SMN02_21f_plg_gl2_g1	64.39	SMN04_21f_plg_gl1_g1	64.32
SMM17_22S	48.33	SMN02_21f_plg_gl2_g1	64.44	SMN04_21f_plg_gl1_g1	64.36
SMM17_22S	48.48	SMN02_21f_plg_gl2_g1	64.65	SMN04_21f_plg_gl1_g1	64.37
SMM17_22S	49.90	SMN02_21f_plg_gl2_g1	64.87	SMN04_21f_plg_gl1_g1	65.07
SMN01_21f_plg_gl1_g1	61.59	SMN02_21f_plg_gl2_g1	64.98	SMN04_21f_plg_gl1_g1	65.12
SMN01_21f_plg_gl1_g1	63.51	SMN02_21f_plg_gl2_g2	54.48	SMN04_21f_plg_gl1_g1	65.63
SMN01_21f_plg_gl1_g1	63.57	SMN02_21f_plg_gl2_g2	55.43	SMN04_21f_plg_gl1_g2	52.50
SMN01_21f_plg_gl1_g1	63.75	SMN02_21f_plg_gl2_g2	55.55	SMN04_21f_plg_gl1_g2	53.55

Table 6 continued.

SMN04_21f_plg_gl1_g2	56.07	SMP07_22S	52.19	SMS02_22S_plg_g3	44.96
SMN04_21f_plg_gl1_g2	57.28	SMP07_22S	54.60	SMS02_22S_plg_g3	49.61
SMN04_21f_plg_gl1_g2	57.91	SMP08_22S	43.45	SMS02_22S_plg_g3	50.07
SMN04_21f_plg_gl1_g2	59.19	SMP08_22S	51.26	SMS02_22S_plg_g3	51.74
SMN04_21f_plg_gl2_g1	62.61	SMP08_22S	64.74	SMS02_22S_plg_g3	53.50
SMN04_21f_plg_gl2_g1	63.58	SMS01_22S_plg_g1	46.24	SMS02_22S_plg_g3	53.60
SMN04_21f_plg_gl2_g1	66.47	SMS01_22S_plg_g1	46.74	SMS03_22S_plg_gl1_g1	42.15
SMN04_21f_plg_gl2_g1	66.80	SMS01_22S_plg_g1	47.01	SMS03_22S_plg_gl1_g1	43.88
SMN04_21f_plg_gl2_g1	67.18	SMS01_22S_plg_g1	47.23	SMS03_22S_plg_gl1_g1	46.41
SMN04_21f_plg_gl2_g1	67.57	SMS01_22S_plg_g1	47.49	SMS03_22S_plg_gl1_g1	47.65
SMN04_21f_plg_gl2_g2	60.40	SMS01_22S_plg_g1	47.93	SMS03_22S_plg_gl1_g1	50.05
SMN04_21f_plg_gl2_g2	61.86	SMS01_22S_plg_gl1_g2	58.58	SMS03_22S_plg_gl1_g1	51.39
SMN04_21f_plg_gl2_g2	61.99	SMS01_22S_plg_gl1_g2	59.06	SMS03_22S_plg_gl1_g2	48.34
SMN04_21f_plg_gl2_g2	62.11	SMS01_22S_plg_gl1_g2	61.04	SMS03_22S_plg_gl1_g2	55.12
SMN04_21f_plg_gl2_g2	63.05	SMS01_22S_plg_gl1_g2	62.11	SMS03_22S_plg_gl1_g2	56.34
SMN04_21f_plg_gl2_g2	63.85	SMS01_22S_plg_gl1_g2	62.32	SMS03_22S_plg_gl1_g2	61.89
SMN05_21f_plg_gl1_g1	59.12	SMS01_22S_plg_gl1_g2	63.55	SMS03_22S_plg_gl1_g2	62.19
SMN05_21f_plg_gl1_g1	60.45	SMS01_22S_plg_gl2_g1	50.14	SMS03_22S_plg_gl1_g2	63.05
SMN05_21f_plg_gl1_g1	60.49	SMS01_22S_plg_gl2_g1	51.08	SMS03_22S_plg_gl2_g1	40.85
SMN05_21f_plg_gl1_g1	61.04	SMS01_22S_plg_gl2_g1	51.84	SMS03_22S_plg_gl2_g1	46.56
SMN05_21f_plg_gl1_g1	62.69	SMS01_22S_plg_gl2_g1	52.58	SMS03_22S_plg_gl2_g1	46.91
SMN05_21f_plg_gl1_g1	63.23	SMS01_22S_plg_gl2_g1	52.90	SMS03_22S_plg_gl2_g1	47.35
SMN05_21f_plg_gl1_g2	54.36	SMS01_22S_plg_gl2_g1	53.21	SMS03_22S_plg_gl2_g1	47.60
SMN05_21f_plg_gl1_g2	54.87	SMS01_22S_plg_gl2_g2	51.43	SMS03_22S_plg_gl2_g1	51.42
SMN05_21f_plg_gl1_g2	56.86	SMS01_22S_plg_gl2_g2	51.68	SMS03_22S_plg_gl2_g2	43.61
SMN05_21f_plg_gl1_g2	57.02	SMS01_22S_plg_gl2_g2	54.17	SMS03_22S_plg_gl2_g2	51.16
SMN05_21f_plg_gl1_g2	59.66	SMS01_22S_plg_gl2_g2	55.15	SMS03_22S_plg_gl2_g2	54.58
SMN05_21f_plg_gl1_g2	60.46	SMS01_22S_plg_gl2_g2	56.90	SMS03_22S_plg_gl2_g2	59.47
SMN05_21f_plg_gl2_g1	53.80	SMS01_22S_plg_gl2_g2	56.93	SMS03_22S_plg_gl2_g2	60.41
SMN05_21f_plg_gl2_g1	54.53	SMS02_22S_plg_g1	39.76	SMS03_22S_plg_gl2_g2	61.68
SMN05_21f_plg_gl2_g1	55.56	SMS02_22S_plg_g1	53.28	SMS04_22S_plg_gl1_g1	38.25
SMN05_21f_plg_gl2_g1	57.48	SMS02_22S_plg_g1	53.92	SMS04_22S_plg_gl1_g1	40.76
SMN05_21f_plg_gl2_g1	57.61	SMS02_22S_plg_g1	58.34	SMS04_22S_plg_gl1_g1	44.11
SMN05_21f_plg_gl2_g1	59.36	SMS02_22S_plg_g1	59.90	SMS04_22S_plg_gl1_g1	46.43
SMN05_21f_plg_gl2_g2	46.48	SMS02_22S_plg_g1	60.12	SMS04_22S_plg_gl1_g1	49.57
SMN05_21f_plg_gl2_g2	51.07	SMS02_22S_plg_g2	41.47	SMS04_22S_plg_gl1_g1	78.09
SMN05_21f_plg_gl2_g2	51.94	SMS02_22S_plg_g2	45.95	SMS04_22S_plg_gl1_g2	50.43
SMN05_21f_plg_gl2_g2	53.60	SMS02_22S_plg_g2	52.98	SMS04_22S_plg_gl1_g2	61.13
SMN05_21f_plg_gl2_g2	54.56	SMS02_22S_plg_g2	53.99	SMS04_22S_plg_gl1_g2	66.20
SMN05_21f_plg_gl2_g2	55.71	SMS02_22S_plg_g2	57.65	SMS04_22S_plg_gl1_g2	68.81
SMP07_22S	50.22	SMS02_22S_plg_g2	58.86	SMS04_22S_plg_gl1_g2	71.85

Table 6 continued.

SMS04_22S_plg_gl1_g2	73.38
SMS04_22S_plg_gl2_g1	56.77
SMS04_22S_plg_gl2_g1	57.61
SMS04_22S_plg_gl2_g1	57.90
SMS04_22S_plg_gl2_g1	58.44
SMS04_22S_plg_gl2_g1	58.58
SMS04_22S_plg_gl2_g1	58.79
SMS04_22S_plg_gl2_g2	62.60
SMS04_22S_plg_gl2_g2	63.14
SMS04_22S_plg_gl2_g2	63.24
SMS04_22S_plg_gl2_g2	63.46
SMS04_22S_plg_gl2_g2	67.24
SMS04_22S_plg_gl2_g2	68.38
SMS05_22S_plg_gl1_g1	61.57
SMS05_22S_plg_gl1_g1	62.99
SMS05_22S_plg_gl1_g1	63.67
SMS05_22S_plg_gl1_g1	65.02
SMS05_22S_plg_gl1_g1	66.49
SMS05_22S_plg_gl1_g1	68.79
SMS05_22S_plg_gl1_g2	37.70
SMS05_22S_plg_gl1_g2	38.33
SMS05_22S_plg_gl1_g2	40.59
SMS05_22S_plg_gl1_g2	41.56
SMS05_22S_plg_gl1_g2	46.76
SMS05_22S_plg_gl1_g2	91.75
SMS05_22S_plg_gl2_g1	46.70
SMS05_22S_plg_gl2_g1	61.01
SMS05_22S_plg_gl2_g1	62.23

SMS05_22S_plg_gl2_g1	65.29
SMS05_22S_plg_gl2_g1	65.52
SMS05_22S_plg_gl2_g1	66.01
SMS05_22S_plg_gl2_g2	44.66
SMS05_22S_plg_gl2_g2	59.64
SMS05_22S_plg_gl2_g2	60.92
SMS05_22S_plg_gl2_g2	60.95
SMS05_22S_plg_gl2_g2	61.71
SMS05_22S_plg_gl2_g2	62.62
SMS06_22S_plg_gl1_g1	36.32
SMS06_22S_plg_gl1_g1	37.02
SMS06_22S_plg_gl1_g1	37.06
SMS06_22S_plg_gl1_g1	43.31
SMS06_22S_plg_gl1_g1	43.77
SMS06_22S_plg_gl1_g1	45.94
SMS06_22S_plg_gl1_g2	48.69
SMS06_22S_plg_gl1_g2	55.49
SMS06_22S_plg_gl1_g2	58.78
SMS06_22S_plg_gl1_g2	60.04
SMS06_22S_plg_gl1_g2	60.09
SMS06_22S_plg_gl1_g2	60.17
SMS06_22S_plg_gl2_g1	40.65
SMS06_22S_plg_gl2_g1	41.45
SMS06_22S_plg_gl2_g1	43.42
SMS06_22S_plg_gl2_g1	43.66
SMS06_22S_plg_gl2_g1	45.00
SMS06_22S_plg_gl2_g1	47.96
SMS06_22S_plg_gl2_g2	41.46

SMS06_22S_plg_gl2_g2	51.92
SMS06_22S_plg_gl2_g2	58.96
SMS06_22S_plg_gl2_g2	60.38
SMS06_22S_plg_gl2_g2	64.30
SMS06_22S_plg_gl2_g2	64.49
SMS07_22S_plg_gl1_g1	62.75
SMS07_22S_plg_gl1_g1	62.82
SMS07_22S_plg_gl1_g1	63.23
SMS07_22S_plg_gl1_g1	63.80
SMS07_22S_plg_gl1_g1	63.91
SMS07_22S_plg_gl1_g1	64.88
SMS07_22S_plg_gl1_g2	41.09
SMS07_22S_plg_gl1_g2	54.38
SMS07_22S_plg_gl1_g2	57.40
SMS07_22S_plg_gl1_g2	58.98
SMS07_22S_plg_gl1_g2	61.34
SMS07_22S_plg_gl1_g2	61.37
SMS07_22S_plg_gl2_g1	42.89
SMS07_22S_plg_gl2_g1	56.53
SMS07_22S_plg_gl2_g1	61.53
SMS07_22S_plg_gl2_g1	65.16
SMS07_22S_plg_gl2_g1	67.41
SMS07_22S_plg_gl2_g1	68.33
SMS07_22S_plg_gl2_g2	43.90
SMS07_22S_plg_gl2_g2	47.57
SMS07_22S_plg_gl2_g2	51.14
SMS07_22S_plg_gl2_g2	51.52
SMS07_22S_plg_gl2_g2	51.78
SMS07_22S_plg_gl2_g2	55.28